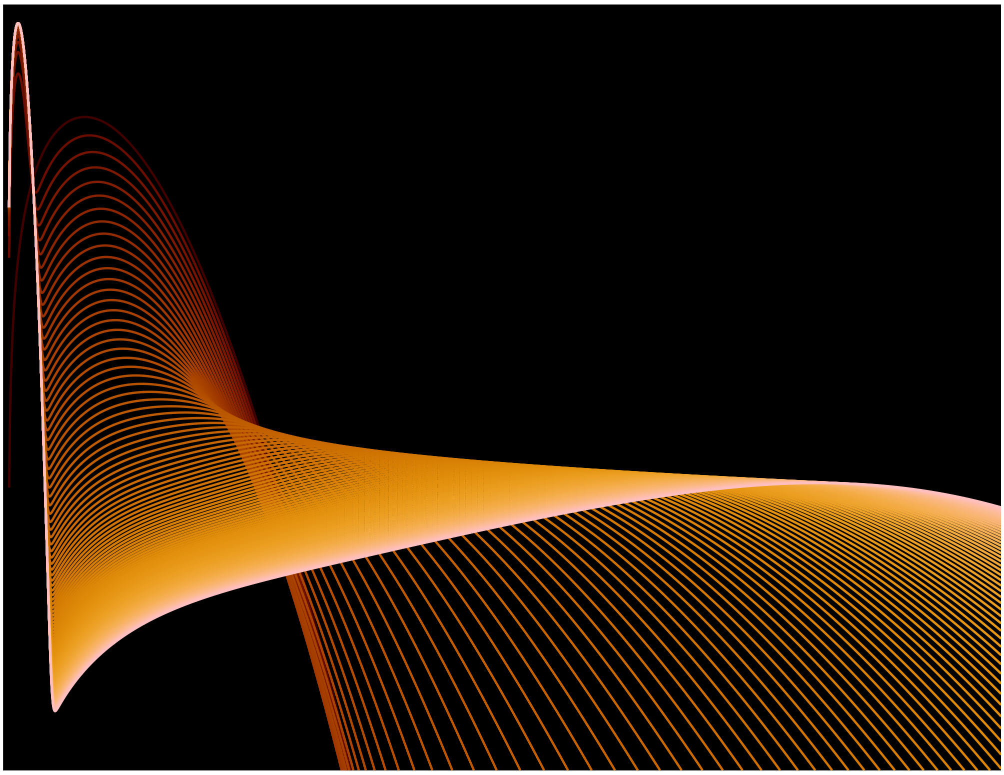

Hot-tail runaway electron generation in cooling fusion plasmas

Thesis for the degree of Master of Science in Applied Physics

IDA SVENNINGSSON

Department of Physics
CHALMERS UNIVERSITY OF TECHNOLOGY
Gothenburg, Sweden 2020

Master's thesis 2020

Hot-tail runaway electron generation in cooling fusion plasmas

IDA SVENNINGSSON

Department of Physics
Division of Subatomic, High Energy and Plasma Physics
Plasma Theory
Chalmers University of Technology
Gothenburg, Sweden 2020

Hot-tail runaway electron generation in cooling fusion plasmas

IDA SVENNINGSSON

Supervisors:	Ola Embréus, Department of Physics
	Sarah Newton, Department of Physics
Examiner:	Tünde Fülöp, Department of Physics

Department of Physics
Division of Subatomic, High Energy and Plasma Physics
Plasma Theory
Chalmers University of Technology
SE-412 96 Gothenburg
Telephone +46 31 772 1000

Cover: Electron momentum distribution function at different points in time as a hot tail is formed, simulated in CODE.

Typeset in LaTeX
Printed by Chalmers Reproservice
Gothenburg, Sweden 2020

Hot-tail runaway electron generation in cooling fusion plasmas

IDA SVENINGSSON
Department of Physics
Chalmers University of Technology

Abstract

Runaway electrons pose a threat to safe operation of magnetic confinement fusion reactors due to the damage they can cause on the reactor wall. During a fast cooling of a fusion plasma, the electric field strength increases and high-energy electrons are accelerated to relativistic speeds, a process called hot-tail runaway generation. To mitigate their effect, reliable and efficient theoretical models to predict generation of hot-tail electrons are of importance. Current numerical methods are computationally expensive and the accuracy of available analytical models has not been found satisfactory. In this work, analytical and simplified numerical models for hot-tail generation including a self-consistent description of the electric field are proposed. The models are benchmarked against numerical simulations and their regions of validity are explored.

Keywords: plasma, runaway, hot-tail, fusion, tokamak disruptions.

Acknowledgements

I have had the privilege of being supervised by Ola, Sarah and Tünde, whose help and encouragement have been extremely valuable in my process of entering a field of physics that was very new to me. First, I want to thank Ola for laying the groundwork for this thesis, for your great intuition, your contagious enthusiasm, and for always thinking one step ahead. I also want to thank Sarah who with her deep knowledge in plasma physics, attention to detail and supportive attitude has taken the quality of this thesis to a new level. Tünde is the one who brought me into plasma physics and has shown incredible support from day one. Thank you for being such an inspiring group leader, especially in times when all work needs to be carried out remotely. Thank you to everyone in the plasma theory group for creating such a warm and happy atmosphere, and special thanks to István Pusztai who proof read this report.

I would also like to thank my parents for giving helpful advice, and my siblings for all the excitement and inside jokes. Thank you also to our lively dog Nimbus, for informative demonstrations on chasing (hot) tails. Finally, I thank my flatmate Truls for the smoothies, for always being curious and never hesitating to ask stupid questions.

Ida Svenningsson, Gothenburg, June 2020

Contents

1
Introduction

The ongoing climate crisis is one of the great challenges of the 21$^{\text{st}}$ century, and to avoid the most severe impacts efforts must be made to transform energy production [1]. One of the possibilities for a future clean energy source is nuclear fusion, but many technical challenges still remain on the way to realization [2]. One of them is understanding and mitigating the effect of so-called runaway electrons, high-energy particles that are generated during fault events and have the potential to cause severe damage to the reactor wall [3]. In this thesis we will model a specific type of runaway generation known as the hot-tail effect, which occurs when the fusion plasma temperature drops rapidly.

1.1 Nuclear fusion

Fusion is the reaction in which light nuclei such as deuterium (^{2}H) and tritium (^{3}H) are fused together to form helium (^{4}He) and a neutron. The light neutron takes up around 80% of the energy released in in the form of kinetic energy, which is harvested as heat to drive a turbine and extract electricity. One of the advantages of nuclear fusion as an energy source is energy density; from the same fuel mass, controlled fusion releases four times the energy released from nuclear fission and almost four million times the energy released from burning fossil fuels such as coal, oil or gas. The fuels needed for a fusion reaction are deuterium, which can be easily extracted from normal seawater, and tritium, which can be produced inside the reactor as fusion neutrons interact with the lithium isotope ^{6}Li. Furthermore, no greenhouse gases or other harmful chemicals are produced by the fusion reaction. Radioactive byproducts are formed when the high-energy neutrons activate the reactor wall, but these are very short-lived compared to fission waste. [4]

For the fusion reaction to take place, the particles need to move fast to overcome the electrostatic repulsion keeping the atomic nuclei apart. This requires extreme temperatures above 100 million degrees Celsius, hotter than the centre of the sun [5]. At such temperatures, the fusion fuel takes the form of a plasma, the state of matter where electrons are separated from the nuclei. No material can endure the heat of a reacting fusion plasma, but it can be contained by magnetic forces. Magnetic confinement is possible because a charged particle moving in a magnetic field experiences a Lorentz force which causes the particle to spiral around the magnetic field lines.

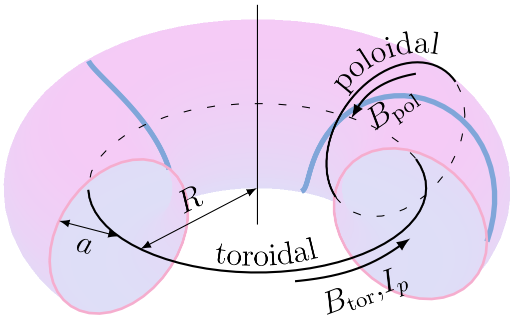

Figure 1.1: A tokamak plasma (pink). The particles approximately follow the magnetic field (blue), which has a twisted trajectory in the toroidal and poloidal direction, and R and a are the major and minor radii.

1.1.1 The tokamak

The tokamak is, along with the stellarator, the most promising candidate to become the first working nuclear fusion reactor [6]. It has the shape of a torus and is a complex construction consisting of superconducting magnets, a vacuum chamber to protect the plasma from contamination and numerous other components. A very simplified illustration of the plasma inside a tokamak is shown in Figure 1.1. The electrons and ions closely follow the magnetic field lines and circulate around the torus. The toroidal magnetic field, B_{tor} is created by external magnets. A purely toroidal magnetic field would not be a stable configuration since the field is larger on the inside edge than on the outside. This gradient in the magnetic field causes the particles to drift approximately vertically, with opposite charges moving in opposite directions. The resulting electric field causes an $\mathbf{E} \times \mathbf{B}$ drift, which moves all charged species radially outwards together, and the plasma confinement is lost. Stable confinement can be provided by twisting the magnetic field. A plasma current I_p is therefore driven through the torus, introducing a poloidal component of the magnetic field, B_{pol}. An example of a twisted magnetic field line is shown in blue in Figure 1.1.

Several tokamaks have already been constructed and shown to successfully create fusion reactions, but a burning plasma, where the energy coming from the fusion reaction is enough to sustain a high temperature, is yet to be achieved. The Q-factor – the amount of generated fusion power divided by the supplied heating power – is a measure of the efficiency of the reactor. For a net energy production, a Q larger than one is required. The highest Q-factor reached to date is $Q = 0.67$ and was achieved in the JET tokamak in the UK [7].

ITER

ITER is a collaboration between 35 nations to build the world's largest tokamak in the south-east of France [2]. Operation is planned to start in 2025. Reaching a central temperature of 150 million degrees Celsius, ITER will, if successful, have a Q-factor of 10, and be the first demonstration of a fusion reactor which produces more energy than it consumes. It is not designed to harvest electricity from the energy it produces, but will work as a demonstration of the possibility to produce net energy and thereby pave the way for a future working fusion reactor. ITER will have a major and minor radius of 6.2 m and 2 m respectively and a plasma current of 15 MA. The plasma is estimated to have a thermal energy of 350 MJ and a poloidal magnetic energy of 395 MJ during operation [8]. In the case of a disruption, which we will discuss in section 1.2.2, this energy is converted to kinetic energy of runaway electrons and is potentially released to the wall in a few milliseconds.

1.2 Runaway electrons

Collisions between charged particles in a plasma happen due to Coulomb interaction and mainly cause small changes in the velocities of the colliding particles. This fundamental property of a plasma causes the collision frequency to *decrease* with increasing velocity, contrary to the behaviour in a neutral gas. The friction on a particle, which is proportional to its collision frequency, therefore also decreases at high velocities. If an electric field is applied, high-energy electrons can thus be accelerated to relativistic speeds and become so-called *runaway electrons*, or *runaways*. The runaway phenomena has been observed in nature as the main cause of lightning initiation in thunder clouds on Earth [9]. It also occurs in numerous astrophysical systems, for example in solar flares and thunderstorms on the gaseous giants in our solar system [10, 11].

The runaway electrons of interest in this thesis are the ones created in laboratory plasmas, more specifically in magnetic confinement fusion reactors. Runaways generated in tokamaks can cause severe damage on the inner wall of the reactor. They have been encountered in many current devices [12, 13, 14, 15, 16], and their importance is only expected to increase in future larger reactors such as ITER, due to higher currents [8].

1.2.1 Runaway mechanisms in tokamaks

Runaway generation in tokamaks can be divided into the two sub-groups: primary and secondary generation. Primary generation is when an electron through the cumulative effect of small-angle collisions gains enough energy to run away. The primary generation that has been the most studied is Dreicer generation [17, 18]. In the presence of a weak electric field, the fastest electrons in the tail of the distribution will experience such a weak friction that they run away. More runaways are also continually created as cold electrons diffuse into the high velocity region through a random-walk process. Hot-tail generation is another example of primary generation, and occurs when the plasma temperature drops rapidly due to a disruption. This is discussed further below.

Runaway electrons can also collide with cold electrons in close, large-angle collisions, which can give both electrons enough energy to run away. This is called avalanche multiplication, and is known as secondary generation. The avalanche process amplifies the “runaway seed”, the runaway population that has been produced by the primary generation processes [19]. The avalanche multiplication effect will be stronger in large tokamaks such as ITER than in current devices [20], and it is thus very important to understand primary runaway generation and reduce the runaway seed.

Hot-tail generation

Due to the lower collision frequency at high velocities, fast particles need longer time to cool than the low energy part of the distribution [21]. A population of hot particles therefore remains after a sudden temperature drop, and can be accelerated by the increased electric field arising during a disruption, causing an increased primary runaway generation. This process is called hot-tail generation, and becomes important when the temperature changes on a timescale shorter than the collision time for high-energy electrons [22, 23, 24, 25, 26].

The hot-tail effect has been observed experimentally in present tokamaks [27, 15, 28], but will be even more relevant in ITER, due to its higher temperature and larger plasma current [15]. For ITER-sized tokamaks, the hot-tail effect is expected to be the dominant primary generation mechanism when the cooling is faster than 1 ms [21]. Since the secondary generation multiplies the runaway seed created by primary generation, quantifying the hot-tail generation is an important part of determining the effect of runaway electrons in a given situation [29, 30]. Simplified modelling of other generation processes have been successful, but measurements of the runaway current created in a disruption suggest that present analytic hot-tail models are not able to accurately predict the hot-tail runaway seed [15].

1.2.2 Tokamak disruptions

Disruptions are dramatic events where the plasma confined in a tokamak loses its magnetic stability. They are usually the consequence of growing magnetohydrodynamic instabilities [8], which occur naturally in the plasma but can also be triggered intentionally for experimental purposes by injection of impurities [31]. During a disruption, thermal energy is lost from the plasma and the temperature drops rapidly in a process called the thermal quench. In ITER, the thermal quench time scale is expected to be of the order of 1 ms [32]. The plasma conductivity depends strongly on the temperature, and therefore also decreases during the thermal quench. Lenz’s law then causes the electric field to grow and maintain the plasma current I_p. This increase in the electric field is central to the runaway problem and will be discussed further in this thesis. The thermal quench is then followed by a current quench, where the plasma current decreases. This happens on a much longer timescale, in ITER predicted around 50 ms. The decay of the plasma current induces halo and eddy currents in the surrounding structures which give rise to forces and local torques that can harm the vessel.

To limit the current quench time, and the potential to damage the tokamak, impurities can be injected into the plasma upon the detection of a disruption [8]. The impurities, which typically consist of neon or argon gas, become partially ionized as they enter the plasma. They can help to control the thermal losses, and act as scattering centres to prevent the buildup of a directed beam of runaway electrons. However, the additional electrons, both free and bound, have been found to have the potential to act as a further source of the runaway beam through avalanche multiplication. Therefore, injection of deuterium in combination with noble gases has been suggested as an alternative mitigation method [20, 33].

1.2.3 Modelling runaway electrons

Electron runaway in fusion plasmas is an extensively studied subject and several numerical models have been developed to simulate how they are generated. One of the most advanced tools is the kinetic solver CODE [34, 35], which will be described further in Section 3.2. CODE computes the time-dependent electron momentum distribution function, from which the density of runaway particles and runaway current generated at a given point in space can be determined as a function of time. CODE has been optimized for computational efficiency, but can still be too time demanding when coupled into full simulations of a disruption. This raises the need for approximate models that calculate the runaway seed at a low computational cost. Such models have been used in disruption simulation frameworks which self-consistently model the radial evolution of, for example, the radiation, plasma current and electric field during a disruption [36, 37, 38, 39]. In this thesis, we will develop improved theoretical models to accurately quantify the hot-tail runaway generation following a disruption.

2

Collisions in plasmas

Collisions between plasma particles are the heart of understanding the runaway phenomenon. In this chapter, we will describe the theory of small-angle collisions, relevant to the problem of hot-tail generation. First, we define relevant plasma properties. Next, we show how the distribution function and the kinetic equation are used to describe the plasma. We then discuss the collision operator describing the small-angle Coulomb collision and give explicit expressions for the electron-ion and electron-electron collision operators. Finally, the relativistic collision operator, which is the one we will employ in Chapter 4, is presented.

2.1 Plasma definition

We define a plasma by the following sentence: *A plasma is a quasineutral gas of charged and neutral particles which exhibits collective behavior* [5]. Quasineutrality means that the plasma can be considered neutral on a macroscopic scale, with the total charge of the plasma adding up to zero:

$$\sum_j Z_j n_j = n_e, \tag{2.1}$$

where j denotes different ion species with charge number Z_j and density n_j and n_e is the electron density. Local potential can build up on short scales, but is shielded out by surrounding particles. If a charge is added to the plasma, particles of the opposite charge will gather around the added charge, which causes the electrostatic potential to decrease exponentially with the distance. This effect is known as Debye shielding and is a fundamental property of a plasma. At distances longer than the Debye length λ_D, Coulomb forces are shielded out and particles do not interact directly. The Debye length is given by

$$\lambda_D = \sqrt{\frac{\epsilon_0 T}{n_e e^2}}. \tag{2.2}$$

For Debye screening to work, the Debye length needs to be much shorter than the typical length scale L of the plasma. For a statistical description to be valid, we also require that the number of particles inside a sphere with radius λ_D is large:

$$\lambda_D \ll L, \quad \frac{4\pi}{3}\lambda_D^3 n_e \gg 1. \tag{2.3}$$

A typical fusion plasma with electron density $n_e = 10^{20}$ m^{-3} and temperature $T = 10^8$ K gives $\lambda_D = 7$ µm and $n_e\lambda_D = 3 \cdot 10^6$, so the conditions (2.3) are satisfied.

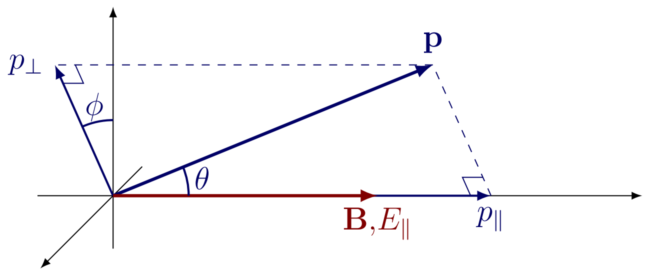

Figure 2.1: Our coordinate system is aligned with the magnetic field. The particle momentum $\mathbf{p}$ is parametrized by $p_\parallel$, the component parallel to the magnetic field, and θ, the pitch-angle, often expressed in the coordinate $\xi = \cos\theta = p_\parallel/p$. The component of the momentum perpendicular to the magnetic field is then $p_\perp$. The gyroangle, ϕ, is also shown.

2.2 Kinetic description of a plasma

The distribution function is useful to describe the collective behavior of the plasma particles. We define the distribution function $f_a(\mathbf{r},\mathbf{p},t)$ so that $f_a(\mathbf{r},\mathbf{p},t)\,\mathrm{d}^3r\,\mathrm{d}^3p$ is the number of particles of species a in the phase space volume element $\mathrm{d}^3r\,\mathrm{d}^3p$ at the time t. The species can be electrons or types of ions. With this definition, the number density of particles in real space is obtained by integrating the distribution function over momentum space:

$$n(\mathbf{r},t) = \int f(\mathbf{r},\mathbf{p},t)\,\mathrm{d}^3p, \tag{2.4}$$

and we see that $f(\mathbf{r},\mathbf{p},t)$ has the dimension (length$\times$momentum)$^{-3}$. In the following we use the relativistic momentum normalized to $m_e c$: $p = \gamma v/c$. The relativistic mass factor γ is related to p through $\gamma^2 = 1 + p^2$. The distribution function is also commonly expressed in terms of velocity, $f(\mathbf{r},\mathbf{v},t)$, in that case with the dimension (length$\times$velocity)$^{-3}$. The two representations are equivalent, and both will be used in this thesis.

Runaway formation is often strongest in the hot core of large fusion plasmas. In this work we will focus on those local conditions and consider an on-axis model by neglecting the spatial dependence. In a magnetized plasma the gyrofrequency is faster than other processes in the system, so the dependency of the gyroangle ϕ is averaged out and can also be neglected. The phase space of the distribution is therefore reduced to a two-dimensional momentum space parametrized in terms of p and the pitch-angle coordinate ξ, defined as the cosine of the angle between $\mathbf{p}$ and the magnetic field. We show this geometry in Figure 2.1. We will from now on suppress the $\mathbf{r}$ and instead write $f(t,p,\xi)$. Relevant quantities such as particle density n and parallel current density $j_\parallel$ are calculated by taking velocity moments of the distribution function in momentum space:

$$n_a(t) = 2\pi \int_{-1}^{1}\int_{0}^{\infty} f_a(p,\xi,t)p^2\,\mathrm{d}p\,\mathrm{d}\xi \tag{2.5}$$

$$j_\parallel(t) = \sum_a \left[2\pi q_a \int_{-1}^{1}\int_{0}^{\infty} v\xi f_a(p,\xi,t)p^2\,\mathrm{d}p\,\mathrm{d}\xi\right], \tag{2.6}$$

where q_a is the charge and a denotes particle species. The distribution function satisfies the Boltzmann equation [5, 40]:

$$\frac{\partial f}{\partial t} + \mathbf{v}\cdot\boldsymbol{\nabla} f + q\left(\mathbf{E}+\mathbf{v}\times\mathbf{B}\right)\cdot\boldsymbol{\nabla}_{\mathbf{p}} f = C(f). \tag{2.7}$$

We will only use the electron distribution function in this thesis, so we will let $q = \text{-}e$ where e is the elementary charge. In the second term, $\boldsymbol{\nabla} f$ is the gradient in real space. This term vanishes since we have no spatial dependence. The third term describes acceleration by external electric and magnetic fields where $\boldsymbol{\nabla}_{\mathbf{p}} f$ is the gradient of the distribution function in momentum space, expressed in spherical coordinates (p,θ,ϕ):

$$\boldsymbol{\nabla}_{\mathbf{p}} f = \frac{\partial f}{\partial p}\hat{p} + \frac{1}{p}\frac{\partial f}{\partial \theta}\hat{\theta} + \frac{1}{p\sin\theta}\frac{\partial f}{\partial \phi}\hat{\phi}. \tag{2.8}$$

Since the gyrofrequency is faster than other processes in the system, the kinetic equation tells us that the distribution function to leading order is independent of ϕ, so $\partial_\phi f = 0$. Therefore we can neglect the final term in this expression of the gradient. We can then rewrite equation (2.7) with the normalized momentum $p = \gamma v/c$ and the pitch-angle coordinate $\xi = \cos\theta$ [34]:

$$\frac{\partial f}{\partial t} + \frac{qE_\parallel}{m_e c}\left(\xi\frac{\partial f}{\partial p} + \frac{1-\xi^2}{p}\frac{\partial f}{\partial \xi}\right) = C_e(f). \tag{2.9}$$

where $E_\parallel$ is the component of the electric field parallel to the magnetic field and $C_e(f)$ is the collision operator which accounts for the effect of particle interactions on the short Debye scale.

2.3 The collision operator

As we are interested in primary runaway generation mechanisms, more reminiscent of Dreicer than avalanche, we use the three-dimensional Fokker-Planck collision operator, which describes the cumulative effect of small-angle Coulomb collisions on the distribution function [40]:

$$C_e(f) = \frac{\partial}{\partial v_k}\Bigg[-\underbrace{\frac{\langle\Delta v_k\rangle}{\Delta t}f}_{\text{slowing-down}} + \underbrace{\frac{\partial}{\partial v_l}\left(\frac{\langle\Delta v_k \Delta v_l\rangle}{2\Delta t}f\right)}_{\text{diffusive spreading}}\Bigg], \tag{2.10}$$

where summation over repeated indexes is implied. The first term in equation (2.10) describes the average change in velocity and typically represents a slowing-down force due to Coulomb collisions. The second term describes random diffusive spreading of the distribution in velocity space. We outline the derivation of the expectation values $\langle \Delta v_k \rangle$ and $\langle \Delta v_k \Delta v_l \rangle$ in Section 2.3.1.

When the background consists of different species, the collision operators for each species are added together. For example, collisions of electrons with both electrons and ions can be written as

$$C_e(f_e) = C_{ee}(f_e,f_e) + C_{ei}(f_e,f_i), \tag{2.11}$$

where $C_{ab}(f_a,f_b)$ should be read as the effect on the distribution f_a of species a due to collisions with species b with the distribution f_b. The full Fokker-Planck collision operator conserves number density of each species, as well as the individual momentum and energy in collisions [40].

The Maxwellian velocity distribution is defined by

$$f_M(\mathbf{v}) = f_M(v) \equiv \frac{n_b}{\pi^{3/2} v_T^3} \exp\left(-v^2/v_T^2\right), \tag{2.12}$$

and is the quasi-equilibrium distribution reached in a tokamak when the slowing-down term and the diffusion term are of equal size. The thermal velocity is defined by $v_T = \sqrt{2T_e/m_e}$, where T_e is the temperature (in plasma physics often measured in units of electronvolts (eV), absorbing Boltzmann's constant k_B into the temperature and writing $k_B T_e \to T_e$), and m_e is the electron mass. This distribution is isotropic, meaning that it is independent of the direction of $\mathbf{v}$. An important feature of the collision operator is that it equals zero when acting on two Maxwellian distributions with the same temperature: $C(f_{Ma},f_{Mb}) = 0$ [40], that is self-collisions in a Maxwellian distribution have no further effect on the distribution function.

The collision operator is bilinear, which means that it obeys the relations

$$C_{ab}(f_a + g_a,f_b) = C_{ab}(f_a,f_b) + C_{ab}(g_a,f_b) \tag{2.13}$$
$$C_{ab}(f_a,f_b + g_b) = C_{ab}(f_a,f_b) + C_{ab}(f_a,g_b) \tag{2.14}$$
$$C_{ab}(c_a f_a,c_b f_b) = c_a c_b C_{ab}(f_a,f_b) \tag{2.15}$$

for any distribution functions f_a, f_b, g_a, g_b, and constants c_a, c_b. This feature will be used to introduce the linearized collision operator in Section 3.2.

2.3.1 Coulomb collisions

When an electron "collides" with another charged particle such as an ion, the electron is deflected by the Coulomb field from the particle, which changes the electron trajectory. Collisional effects in a plasma relevant for Dreicer and hot-tail generation are due to the accumulated effect of many small-angle deflections [5].

We will now consider the mathematical description of a Coulomb collision by looking at a collision between an electron and an ion. The change in velocity of the ion is negligible due to the large ion-electron mass ratio and it can therefore be assumed

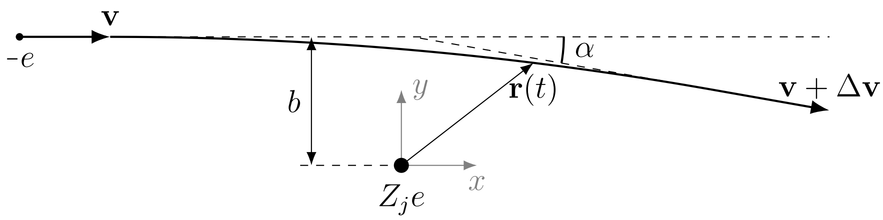

Figure 2.2: Coulomb collision between a heavy, stationary ion with charge $Z_j e$ and an electron with charge -e. Due to Coulomb attraction between the particles, the electron trajectory is changed with the deflection angle α.

fixed in space. As is shown in Figure 2.2, the electron has an initial velocity of $\mathbf{v} = v_x\hat{x}$ and has a perpendicular distance to the ion equal to b. The distance b is called the impact parameter, and would be the distance of closest approach between the particles in the absence of Coulomb forces. The Coulomb force acting on the electron is

$$m_e\mathbf{a}(t) = \mathbf{F}(t) = -\frac{Z_j e^2}{4\pi\epsilon_0}\frac{\mathbf{r}(t)}{r(t)^3}, \tag{2.16}$$

where $\mathbf{r}(t) = x\hat{x} + b\hat{y}$ is the position of the electron relative to the ion. The Coulomb force from the ion changes the electron trajectory with the deflection angle α. In a small angle collision, the change of velocity along the x direction is negligible. If we define $t = 0$ as the point when $x = 0$, the distance between the particles is therefore $r(t) = (b^2 + v^2t^2)^{1/2}$. We can derive the relationship between the impact parameter and the deflection angle by integrating the Coulomb force on the particle and calculating $\Delta\mathbf{v}$:

$$m_e\Delta v_y = \int_{-\infty}^{\infty}\mathbf{F}(t)\cdot\hat{y}\,\mathrm{d}t = -\frac{Z_j e^2}{4\pi\epsilon_0}\int_{-\infty}^{\infty}\frac{b\,\mathrm{d}t}{(b^2+v^2t^2)^{3/2}} = -\frac{Z_j e^2}{2\pi\epsilon_0 bv}. \tag{2.17}$$

Using $\sin\alpha \simeq \alpha$ and $\cos\alpha - 1 \simeq -\alpha^2/2$, we can then write the deflection angle:

$$\alpha \simeq \frac{|\Delta v_y|}{v} = \frac{Z_j e^2}{2\pi\epsilon_0 b m_e v^2}. \tag{2.18}$$

Note that the deflection is smaller when the electron speed, v, is high. We can see this as the electron spending a shorter time in the ion's Coulomb field, and it is therefore less affected by the collision. The changes in parallel and perpendicular velocity caused by the collision are given by:

$$\Delta v_\parallel \simeq v(\cos\alpha - 1) \simeq -\left(\frac{Z_j e^2}{2\pi\epsilon_0 m_a}\right)^2\frac{1}{2b^2v^3} \tag{2.19}$$

$$\Delta v_\perp \simeq v\sin\alpha \simeq -\frac{Z_j e^2}{2\pi\epsilon_0 m_a}\frac{1}{bv}. \tag{2.20}$$

This can be generalized to particles with arbitrary masses, for example two electrons, by using a very similar approach in the center-of-mass frame of the particles.

The velocity changes are then transformed into a global coordinate system. The expectation values needed for the collision operator in equation (2.10) are calculated by integrating with the distribution function over velocities and impact parameters, [40]

$$\frac{\langle \Delta v_k \rangle}{\Delta t} = -\left(\frac{Z_j e^2}{m_e \epsilon_0^2}\right)^2 \frac{\ln \Lambda}{4\pi} \left(1 + \frac{m_e}{m_i}\right) \int \frac{u_k}{u^3} f_b(\mathbf{v}')\, \mathrm{d}^3 v' \tag{2.21}$$

$$\frac{\langle \Delta v_k \Delta v_l \rangle}{\Delta t} = \left(\frac{Z_j e^2}{m_e \epsilon_0^2}\right)^2 \frac{\ln \Lambda}{4\pi} \int \left(\frac{\delta_{kl}}{u} - \frac{u_k u_l}{u^3}\right) f_b(\mathbf{v}')\, \mathrm{d}^3 v', \tag{2.22}$$

where $\mathbf{u} = \mathbf{v} - \mathbf{v}'$ is a relative velocity and δ is the Kronecker delta. The values of the integrals depend on the distribution function of the scattering centres, also called the background distribution, f_b. In Sections 2.3.2, 2.3.3 and 2.3.4 we show examples of the collision operator when the background consists of stationary ions and electrons with a Maxwellian velocity distribution.

The Coulomb logarithm

The integrals over $1/b$ in equations (2.21) and (2.22) need to be cut off since they would diverge as $b \to 0$ and $b \to \infty$. The upper limit is taken as the Debye length λ_D, given in equation (2.2), since Coulomb interaction at longer distances is blocked by Debye shielding. The lower limit is $b_{\min} = \frac{e_i e_e}{2\pi \epsilon_0 m_e v_{Te}^2}$, which is the impact parameter which gives a 90° deflection angle for thermal electrons. When the integral is evaluated, the Coulomb logarithm appears:

$$\ln \Lambda = \ln \frac{\lambda_D}{b_{\min}}. \tag{2.23}$$

The Coulomb logarithm is a measure of how much small-angle collisions dominate over large-angle collisions in a plasma [41, 42]. In a fusion plasma, $\ln \Lambda$ is typically between 15 and 20 [4].

2.3.2 Lorentz gas approximation, electron-ion collisions

When electrons collide with ions, the velocity of the ions is, in general, very low compared to the thermal velocity of the electrons. This is because of the large mass ratio between ions and electrons, which gives $v_{Ti} \ll v_{Te}$ unless the temperatures are very different. The ions can therefore be approximated as stationary. This is strictly valid in the Lorentz limit, where $Z_j \to \infty$. The collision operator for electrons colliding only with fixed ions is, written in spherical coordinates, [40]

$$C_{ei}(f_e) = \frac{n_j Z_j^2 e^4 \ln \Lambda}{4\pi \epsilon_0^2 m_e^2 v^3} \frac{1}{2} \left(\frac{1}{\sin\theta} \frac{\partial}{\partial \theta} \left[\sin\theta \frac{\partial f_e}{\partial \theta}\right] + \frac{1}{\sin^2\theta} \frac{\partial^2 f_e}{\partial \phi^2}\right) \equiv \nu_{ei}(v) \mathscr{L}(f_e), \tag{2.24}$$

where $\nu_{ei}(v)$ is the electron-ion collision frequency and $\mathscr{L}(f)$ is the Lorentz operator, which in the absence of ϕ-dependence is called the pitch-angle scattering operator and can be expressed in terms of the pitch-angle coordinate $\xi = \cos\theta$ as

$$\mathscr{L}(f) = \frac{1}{2} \frac{\partial}{\partial \xi} \left[\left(1 - \xi^2\right) \frac{\partial f}{\partial \xi}\right]. \tag{2.25}$$

The scattering operator is proportional to the angular part of a Laplacian, meaning that it describes diffusion on a sphere with constant energy. Electron-ion collisions conserve the speed of the electrons and only affect the direction of $\mathbf{v}$ by making the distribution function more isotropic. This is called pitch-angle scattering.

When the plasma consists of multiple ion species j with the charge $Z_j e$, the collision frequencies are added to form the total electron-ion deflection collision frequency

$$\nu_D^{ei} = \frac{n_e Z_{\text{eff}} e^4 \ln \Lambda}{4\pi\epsilon_0^2 m_e^2 v^3}. \tag{2.26}$$

Z_{eff} is the effective ion charge, which is the effective charge of a single ion species felt by the electrons due to the combined contribution of all ions in the plasma:

$$Z_{\text{eff}} = \frac{1}{n_e}\sum_j n_j Z_j^2 = \frac{\sum_j n_j Z_j^2}{\sum_j n_j Z_j}, \tag{2.27}$$

where the last equality holds because a plasma is quasineutral, see Section 2.1.

Spitzer conductivity

The plasma conductivity can be derived in the Lorentz approximation by considering the electron distribution in a plasma that has been slightly perturbed away from an initial stationary equilibrium Maxwellian by the application of a weak electric field, so that the distribution is $f_e = f_M + f_{e1} \approx f_M$, where f_{e1} is a small, anisotropic correction to f_M [43]. Under the influence of the electric field $\mathbf{E}$ during a short time Δt, the electrons are accelerated at the rate $-e\mathbf{E}/m_e$, so the velocity distribution changes to

$$f_e(\mathbf{v},t) = f_e\left(\mathbf{v} + \frac{e\mathbf{E}}{m_e}\Delta t, t - \Delta t\right) \tag{2.28}$$

$$\Rightarrow \quad \left(\frac{\partial f_e}{\partial t}\right)_E = \frac{e\mathbf{E}}{m_e}\cdot\frac{\partial f_M}{\partial \mathbf{v}}, \tag{2.29}$$

where f_e was replaced by f_M on the right-hand side since $f_{e1} \ll f_M$. A new equilibrium can be established in which the acceleration is balanced out by collisional drag from ions, given by the electron-ion collision operator in equation (2.24). The correction f_{e1} must be used in the collision operator since collisions have no further effect on the Maxwellian distribution:

$$-\frac{e\mathbf{E}}{m_e}\cdot\frac{\partial f_M}{\partial \mathbf{v}} = \left(\frac{\partial f_{e1}}{\partial t}\right)_{\text{coll}}. \tag{2.30}$$

This has the solution

$$f_{e1} = -\frac{4\pi\epsilon_0^2 m_e^2}{n_e Z_{\text{eff}}} v^4 E f_M \cos\theta. \tag{2.31}$$

The only part of the electron distribution contributing to a net current is the anisotropic f_{e1}. The current density in the direction of the electric field then becomes

$$j = -e \int v \cos\theta f_{e1} \, \mathrm{d}^3 v = \frac{32\pi^{1/2}\epsilon_0^2 (2T_e)^{3/2}}{m_e^{1/2} Z_{\text{eff}} e^2 \ln\Lambda} E \equiv \sigma E. \tag{2.32}$$

With Ohm's law $j = \sigma E$, this gives an expression for the conductivity, σ, of the plasma, known as the parallel Spitzer conductivity derived in the Lorentz limit $Z_{\text{eff}} \to \infty$. The conductivity is lower for finite Z_{eff}, when electron-electron collisions are incorporated, since these provide friction drag on the high velocity tail of the distribution [43, 44]. The conductivity is therefore corrected with the factor $L_{11}(Z_{\text{eff}})$ to give the Spitzer conductivity for arbitrary Z_{eff} [40, 44]:

$$\sigma_{\parallel}^{\text{Sp}} = \frac{12\pi^{3/2}\epsilon_0^2 T_e^{3/2}}{\sqrt{2m_e} Z_{\text{eff}} e^2 \ln\Lambda} L_{11}(Z_{\text{eff}}) \tag{2.33}$$

$$L_{11}(Z_{\text{eff}}) \simeq \frac{1 + 2.966 Z_{\text{eff}} + 0.753 Z_{\text{eff}}^2}{1 + 1.198 Z_{\text{eff}} + 0.222 Z_{\text{eff}}^2}. \tag{2.34}$$

In the Lorentz limit, $L_{11}(Z_{\text{eff}}) = 32/3\pi \approx 3.2$ and the value derived in equation (2.32) is obtained. A noteworthy property of the Spitzer conductivity is that it is essentially density-independent except for a weak logarithmic dependence in the Coulomb logarithm. One might expect the current density caused by a given electric field to increase with the density of charge carriers, n_e. This effect is however counteracted by the increased collisional friction from the raised ion density n_i. Therefore, $\sigma_{\parallel}^{\text{Sp}}$ is proportional to $n_e/n_i = 1/Z_{\text{eff}}$ [43]. Also note the strong temperature dependence since $\sigma_{\parallel}^{\text{Sp}}$ is proportional to $T_e^{3/2}$. As discussed in Chapter 1, this temperature sensitivity is the origin of the hot-tail runaway problem in tokamaks.

2.3.3 Collisions with a Maxwellian background

More generally, in addition to ions, which we still take here to be stationary, we will also consider collisions with electrons. When the background electrons have a Maxwellian velocity distribution, defined by equation (2.12), the test-particle collision operator acting on the electron distribution is [40]

$$C_e(f_e) = \nu_D \mathscr{L}(f_e) + \frac{1}{v^2}\frac{\partial}{\partial v}\left[v^3\left(\nu_S f_e + \frac{1}{2}\nu_{\parallel} v \frac{\partial f_e}{\partial v}\right)\right]. \tag{2.35}$$

The deflection frequency ν_D determines how quickly the distribution is spread out in the angular direction through pitch-angle scattering, the slowing-down frequency ν_S describes how much the electrons are decelerated by collisional friction and the energy diffusion frequency $\nu_{\parallel}$ describes diffusive spreading of the speed v. These three collision frequencies are given by

$$\nu_D = \nu_D^{ee} + \nu_D^{ei} = \frac{\nu_{ee}}{x_e^3}\left(\phi(x_b) - G(x_b) + Z_{\text{eff}}\right) \qquad \text{pitch-angle scattering} \tag{2.36}$$

$$\nu_S = \nu_S^{ee} = \frac{\nu_{ee}}{x_e} 2G(x_b) \qquad \text{collisional friction} \tag{2.37}$$

$$\nu_\parallel = \nu_\parallel^{ee} = \frac{\nu_{ee}}{x_e^3} 2G(x_b) \qquad \text{energy diffusion} \tag{2.38}$$

$$\nu_{ee} = \frac{n_e e^4 \ln\Lambda}{4\pi\epsilon_0^2 m_e^2 v_{Te}^3}, \tag{2.39}$$

where $x = v/v_T$, v_T is the thermal velocity and subscript b denotes the background electrons. The functions $G(x)$ and $\phi(x)$ are the Chandrasekhar and error functions, defined by

$$G(x) = \frac{\phi(x) - x\phi'(x)}{2x^2} \longrightarrow \begin{cases} \frac{2x}{3\sqrt{\pi}}, & x \to 0 \\ \frac{1}{2x^2}, & x \to \infty \end{cases} \tag{2.40}$$

$$\phi(x) = \frac{2}{\sqrt{\pi}} \int_0^x e^{-z^2}\,\mathrm{d}z \equiv \operatorname{erf}(x). \tag{2.41}$$

The Chandrasekhar function $G(x)$ is non-monotonic and decreases when the velocity of the background particles goes above the thermal velocity v_T. At high velocities $x \gg 1$, $G(x)$ approaches the asymptote $1/(2x^2)$. Since the slowing-down frequency is proportional to $G(x)$, the friction on a particle will decrease at high velocities and allow the runaway effect which will be discussed in Chapter 3. Furthermore, we recall from Section 2.3.2 that collisions with ions only contribute to pitch-angle scattering, and therefore only show up in ν_D. The thermal collision frequency for electron-electron collisions is given in equation (2.39). We also define the thermal collision time for electrons as

$$\tau_{ee} = \frac{1}{\nu_{ee}} = \frac{4\pi\epsilon_0^2 m_e^2 v_T^3}{n_e e^4 \ln\Lambda}. \tag{2.42}$$

We can see τ_{ee} as the average time between two collisions for an electron travelling through a plasma with the temperature T.

2.3.4 Relativistic Fokker–Planck operator

When describing high-energy particles such as runaway electrons, we need to use a relativistic collision operator, which can be understood as a generalization of the form in equation (2.35) above. The relativistic collision operator is given by [42]

$$C^{\text{eb,rel}} = \nu_D^{\text{rel}} \mathscr{L}(f_e) + \frac{1}{p^2}\frac{\partial}{\partial p}\left[p^3\left(\nu_S^{\text{rel}} f_e + \frac{1}{2}\nu_\parallel^{\text{rel}} p \frac{\partial f_e}{\partial p}\right)\right], \tag{2.43}$$

expressed in the normalized relativistic momentum $p = \gamma v/c$. The collision frequencies are given by [42, 45, 46]

$$\nu_D^{\mathrm{rel}} = \frac{1}{\tau_c}(1 + Z_{\mathrm{eff}})\frac{\gamma}{p^3} \tag{2.44}$$

$$\nu_S^{\mathrm{rel}} = \frac{1}{\tau_c}\frac{\gamma^2}{p^3} \tag{2.45}$$

$$\nu_\parallel^{\mathrm{rel}} = \frac{1}{\tau_c}\frac{v_T^2}{c^2}\frac{\gamma^3}{p^5}, \tag{2.46}$$

where τ_c is the collision time for relativistic electrons, given by

$$\tau_c = \frac{4\pi\epsilon_0^2 m_e^2 c^3}{n_e e^4 \ln\Lambda}. \tag{2.47}$$

When $T \ll m_e c = 511$ keV, the energy diffusion term $\nu_\parallel^{\mathrm{rel}}$ is negligible. The kinetic equation (2.9) with the collision operator (2.43) can then be simplified to

$$\boxed{\tau_c\frac{\partial f}{\partial t} + \frac{\tau_c e E_\parallel}{m_e c}\left(\xi\frac{\partial f}{\partial p} + \frac{1-\xi^2}{p}\frac{\partial f}{\partial \xi}\right) = \frac{1}{p^2}\frac{\partial}{\partial p}\left[\bar{\nu}_S\gamma^2 f\right] + \bar{\nu}_D\frac{\gamma}{p^3}\mathscr{L}(f),} \tag{2.48}$$

where the collision frequencies are normalized so that $\bar{\nu}_S = 1$ and $\bar{\nu}_D = 1 + Z_{\mathrm{eff}}$. This version of the kinetic equation is the one we will solve in the analytic derivations in Chapter 4.

Effect of partially ionized impurities

In a cold post-disruption plasma, impurity ions will have a low ionization degree. Partially ionized impurities have electrons bound to the nucleus which shield out parts of the ion charge. Electrons with low energy thus only see the net charge of the ion. If the electrons have enough speed, however, they are able to penetrate the cloud of bound electrons and experience the full nuclear charge; fast electrons are less affected by screening. Recent work [47] has incorporated the effects of screening from partially ionized impurities into the collision frequencies appearing in the relativistic collision operator (2.48). In the ultra-relativistic limit $p \gg 1$ the corrections to $\bar{\nu}_S$ and $\bar{\nu}_D$ are given by [45]

$$\bar{\nu}_S \approx 1 + \frac{1}{\ln\Lambda}\sum_j \frac{n_j}{n_e}N_{e,j}\left(\ln I_j^{-1} - 1\right) + \ln p\frac{1}{2\ln\Lambda}\left(1 + 3\sum_j\frac{n_j}{n_e}N_{e,j}\right) \tag{2.49}$$

$$\bar{\nu}_D \approx 1 + Z_{\mathrm{eff}} + \frac{1}{\ln\Lambda}\sum_j\frac{n_j}{n_e}\left(\left(Z_j^2 - Z_{0,j}^2\right)\ln\bar{a}_j - \frac{2}{3}N_{e,j}^2\right) + \ln p\frac{1}{\ln\Lambda}\sum_j\frac{n_j}{n_e}Z_j^2, \tag{2.50}$$

and can also be written in the form $\bar{\nu}_S \approx \bar{\nu}_{S0} + \bar{\nu}_{S1}\ln p$ and $\bar{\nu}_D \approx \bar{\nu}_{D0} + \bar{\nu}_{D1}\ln p$. Here, $Z_{0,j}$ is the ionization state, $N_{e,j} = Z_j - Z_{0,j}$ is the number of bound electrons of nucleus of species j and I_j is the mean excitation energy of the ion normalized to the rest energy. The effective ion size $\bar{a}_j$ depends on ion species and ionization degree and can be determined by density functional theory (DFT) calculations.

3
Runaway electrons

We saw in the previous chapter that the collisional friction which slows down the plasma particles decreases when the velocity is above a certain value. This allows the fastest electrons in the distribution to be accelerated to relativistic speeds when an external electric field is applied and – *run away.* In this chapter, the runaway phenomena is described in Section 3.1. In this thesis we focus on the hot-tail runaway generation, which occurs during quick cooling of a plasma, and this is described in detail in Sections 3.1.1 and 3.1.2. We move on to describe the numerical tool CODE, which we use to model runaway generation, in Section 3.2. Finally, in Section 3.3 we describe two models which have been proposed in the literature. These have been found to not generally capture the resulting runaway number well, and therefore the focus in Chapter 4 will be formulating improved descriptions of the hot-tail process.

3.1 Runaway electrons

The collisional drag which slows down a particle due to the cumulative effect of Coulomb collisions is proportional to the slowing-down frequency ν_S and given by

$$F_{ee,\|} = \frac{m_e \left\langle \Delta v_\| \right\rangle}{\Delta t} = -m_e v_\| \nu_S \propto G\left(\frac{v_b}{v_T}\right), \tag{3.1}$$

where $v_\| = \xi v$ is the component of the velocity parallel to the magnetic field. This force is proportional to the so-called Chandrasekhar function $G(x)$, defined by equation (2.40) and illustrated in Figure 3.1. Since $G(x) \to 0$ as $x \to \infty$, the friction force vanishes at high velocities. An external electric field will accelerate the electrons with the force eE. However weak, it will always be stronger than the friction force on the fastest electrons in the distribution if relativistic effects are ignored. In Figure 3.1, the critical velocity above which this occurs is denoted v_c. These electrons will be accelerated to very high velocities and become so-called runaway electrons. A sufficiently strong field overcomes the friction on the thermal electrons ($v_c = v_T$), which causes all electrons to experience the runaway effect. This occurs when E exceeds the Dreicer field E_D, defined as $eE_D = F_{ee,\|}(v = v_T)$ and given by [17]

$$E_D = \frac{n_e e^3 \ln\Lambda}{4\pi\epsilon_0^2 T_e}. \tag{3.2}$$

If relativistic effects are considered, the friction will not fall all the way to zero when the velocity approaches the speed of light c. The critical field below which no

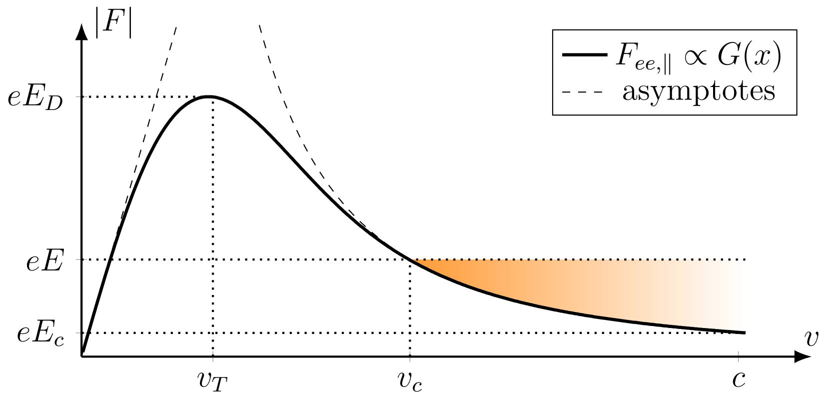

Figure 3.1: Forces associated with electron runaway. The collisional drag force, $F_{ee,\parallel}$, is proportional to the non-monotonic Chandrasekhar function $G(x)$ and decreases for high velocities $v > v_T$. The gray region $v > v_c$ is where the acceleration from the electric field overcomes the friction and the electrons run away.

runaway occurs is therefore given by $eE_c = F_{ee,\parallel}(v \to c)$ and equals [48]

$$E_c = \frac{m_e c}{e\tau_c} = \frac{n_e e^3 \ln\Lambda}{4\pi\epsilon_0^2 m_e c^2}. \tag{3.3}$$

The critical speed v_c above which the electric field overcomes the friction defines the runaway region, where particles with $v < v_c$ will be slowed down and those with $v > v_c$ will run away. The number of electrons per volume expected to run away, the so-called runaway density n_{RE}, is calculated by integrating the distribution function over the runaway region in velocity space

$$n_{\mathrm{RE}} = \int\limits_{v>v_c} f \,\mathrm{d}^3 v. \tag{3.4}$$

A first expression for the critical momentum above which runaway electrons are generated was calculated from the assumption that all electrons move parallel to the electric field, and reads [48]

$$p_c = \frac{1}{\sqrt{E_\parallel / E_c - 1}}. \tag{3.5}$$

For strong electric fields $E \gg E_c$, this can be approximated by $p_c \approx \sqrt{E_c/E_\parallel}$. In general in a magnetized plasma the runaway region will depend on the pitch-angle coordinate ξ, since electrons that initially do not travel along the electric field are less likely to run away. A pitch-angle dependent runaway region can be derived by looking at particle trajectories in 2D momentum space (p,ξ) [29]. The collisionless electron trajectory through the point $p = p_c$, $\xi = 1$ is a separatrix which separates the momentum space into a thermal and a runaway region with very different dynamical properties. Exactly along this trajectory the electron is neither accelerated nor slowed down, but outside it will be accelerated and run away. By considering the kinetic equation in the limit of high critical momentum

$p_c \gg p_T = \gamma v_T/c$ and no velocity diffusion or pitch-angle scattering (neglecting $\nu_\parallel$ and ν_D), such a separatrix is found to be [24]

$$p_{\text{sep}}(\xi) = \sqrt{\frac{2}{1+\xi}}\sqrt{\frac{E_c}{E_\parallel}}. \tag{3.6}$$

Equation (3.6) is often used to approximate the lower boundary of the runaway region, since the "real" separatrix depends on more parameters and cannot be calculated analytically.

As mentioned in Chapter 1, runaway electrons are caused by different mechanisms. Primary generation includes the Dreicer and hot-tail mechanisms, tritium β-decay, and Compton scattering of γ-rays emitted by the activated tokamak walls [39]. Dreicer generation, which involves diffusion of electrons into the runaway region, has been well described by a solution of the kinetic equation with asymptotic expansion in the case of a fully ionized plasma [48]. Recent work has also presented a neural network which predicts the Dreicer generation generation rate in the presence of partially ionized impurities [49]. Secondary generation, commonly referred to as avalanche multiplication, is caused by close, large-angle collisions between existing runaways and thermal electrons, and is given by $n_{\text{RE}}^{\text{ava}} = n_{\text{seed}} \exp(N_{\text{ava}})$ with N_{ava} the logarithm of the avalanche multiplication factor and n_{seed} the runaway seed from primary generation [33, 50].

A useful way to quantify the importance of runaway generation in a given scenario is to calculate the runaway fraction, defined as the ratio between the runaway density n_{RE} and the initial electron density n_0. In Chapter 5, this is the quantity used to compare how well our approximations reproduce numerical results. Another commonly used quantity is the current conversion, which measures how large a fraction of the plasma current ends up as runaway current.

3.1.1 Hot-tail generation

The focus in this thesis is on the hot-tail runaway generation. The hot-tail effect occurs when the plasma temperature drops so quickly that some electrons do not have time to slow down. Such a scenario arises in tokamak plasmas, as noted in the introduction, and in the next section we describe in more detail that cooling process. With the collision time given by equation (2.42) being proportional to v^3, the fastest electrons experience so little collisional drag force that they keep their high speed when the slower electrons are cooled down. This process is illustrated in Figure 3.2. The distribution starts as a Maxwellian with temperature T_{initial}. The temperature is then dropped to T_{final} much lower than T_{initial}. The cold electrons have a short collision time and are cooled down almost instantly, represented by the thin peak close to $p = 0$ in Figure 3.2(b). The electrons with a higher initial velocity take longer to cool down since their collisions are less frequent.

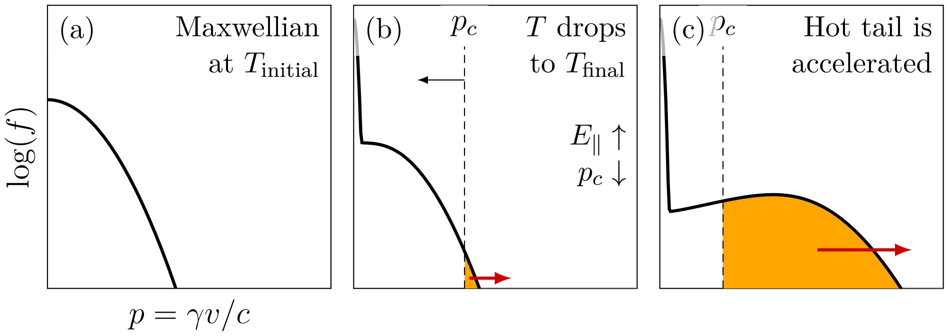

Figure 3.2: The distribution function at different stages during hot-tail generation. Initially, the electrons have a Maxwellian distribution at T_{initial} and the electric field is weak. The temperature then drops rapidly to $T_{\text{final}} = 0.005 T_{\text{initial}}$. This causes the electric field to rise which lowers the critical momentum for runaway generation, p_c.

Recall that the Spitzer conductivity in equation (2.33), which is proportional to $T^{3/2}$, decreases when the temperature drops. Any plasma current is prevented by the plasma inductance from changing on such short time scales and is essentially constant during the cooling [24]. To make up for the loss of conductivity, the electric field rises to maintain constant current through $j = \sigma E$. When the electric field increases, the critical momentum p_c (see equation (3.5)) decreases. This increases the number of electrons arriving in the runaway region, which are then accelerated and form a hot tail in the distribution, as we can see in Figure 3.2(c).

3.1.2 Thermal quench

A disruption, that is a sudden loss of magnetic confinement in a tokamak, is typically accompanied by a rapid cooling of the plasma, often referred to as the thermal quench. The details of the thermal quench are not known, and the cooling mechanisms as well as the temperature profile vary between reactors and experiments [31]. Hence, the temperature evolution needs to be approximated when modelling hot-tail generation, either by assuming a pre-determined cooling profile or calculating the temperature self-consistently accounting for relevant cooling mechanisms. Recent experimental and simulation results show that the duration of the thermal quench significantly affects the runaway generation [28, 30].

The two main mechanisms operating during the thermal quench are line-radiation and heat transport [31]. Radiation losses are caused by ionization of impurity atoms which have entered the plasma, either by influx or intentional injection. Impurity injection is used to experimentally trigger disruptions, either for study or mitigation, and is often accomplished by injecting pellets of argon or neon [28], which evaporate and the atoms are released as the pellet travels through the plasma. In disruptions triggered by such pellets, it has been observed experimentally that the time scale of the thermal quench depends on the pre-disruption plasma temperature [28]. The temperature dropped significantly faster at high temperatures, which may be counterintuitive since a hot plasma should be expected to take longer to cool down. The proposed explanation is that the pellets evaporate more quickly, which releases more impurities into the plasma, triggers a faster cooling and more runaways. Simulations of ITER-like scenarios have also shown that increased impurity density generates a faster thermal quench [51]. In disruptions, heat transport losses are typically due to magnetohydrodynamic instabilities which cause a stochastization of the magnetic field lines [31].

When prescribing a temperature evolution for the thermal quench, a common assumption is an exponential-like temperature decay [21, 24, 25, 30]. This is physically motivated by assuming radiation to be the main cooling mechanism. An exponential temperature evolution, defined by equation (3.14), is used in the model we will describe in Section 3.3.1. A model where the temperature evolution due to radiation is calculated self-consistently together with the distribution function is described in Section 3.3.2. In the derivations in Chapter 4, we use a very fast cooling represented by a step function from T_{initial} to some final temperature T_{final}. This is done to simplify the analysis since the objective is to find an analytical expression for the hot-tail seed generation.

3.2 CODE, a numerical Fokker–Planck solver

The numerical tool CODE, COllisional Distribution of Electrons, written in MATLAB, calculates the time-dependent electron distribution function by solving the kinetic equation (2.9) [34, 35]. It uses a fully relativistic collision operator valid for both low and high velocities, which in the nonrelativistic limit $v \ll c$ reduces to equation (2.35) [52]. CODE is the most exact way of modeling the kinetics of runaway generation used in this thesis, and will be taken to give the reference value when checking the validity of our more approximate models.

Linearized collision operator

From bilinearity of the collision operator mentioned in Section 2.3, it follows that the electron-ion part of the collision operator is linear: $C_{ei}(c_e f_e, f_i) = c_e C_{ei}(f_e, f_i)$, as for any unlike species collisions. However self-collisions are always nonlinear: $C_e(c_e f_e) = C_{ee}(c_e f_e, c_e f_e) = c_e^2 C_{ee}(f_e, f_e)$. In CODE, the operator is linearized by assuming the electron distribution function to be in large part approximately a Maxwellian, so that it can be written as the sum $f_e = f_M + f_{e1}$ where $f_{e1} \ll f_M$, and f_M is a Maxwellian distribution defined by equation (2.12). The electron-electron part of the collision operator can then be approximated by

$$\begin{aligned} C_{ee}(f_e, f_e) &= C_{ee}(f_M + f_{e1}, f_M + f_{e1}) \\ &\approx C_{ee}(f_M, f_{e1}) + C_{ee}(f_{e1}, f_M) \equiv C_{ee}^l(f_e). \end{aligned} \tag{3.7}$$

Here, the quadratic term $C_{ee}(f_{e1}, f_{e1})$ is neglected and $C_{ee}(f_M, f_M) = 0$ since the Maxwellian is unaffected by the Coulomb collision operator. Just like the full collision operator, the linearized collision operator $C_{ee}^l(f_e)$ conserves number of particles, momentum and energy [40]. Moreover, the angular eigenfunctions of the collision operator (3.7) are the Legendre polynomials $P_L(\xi)$, $\xi = \cos\theta$, given by

$$P_L(\xi) = \frac{1}{2^L L!}\frac{\mathrm{d}^L}{\mathrm{d}\xi^L}\left(\xi^2 - 1\right)^L, \tag{3.8}$$

and of which the first three are $P_0(\xi) = 1$, $P_1(\xi) = \xi$ and $P_2(\xi) = \frac{1}{2}(3\xi^2 - 1)$. In CODE, the distribution function is therefore expanded in N_ξ Legendre modes $f_L(p)$: [29, 34]

$$f(t,p,\xi) = \sum_{L=0}^{N_\xi-1} f_L(t,p)P_L(\xi). \tag{3.9}$$

The linearization of the collision operator and the Legendre decomposition of the distribution function allow for cheap time advancement, since the matrix describing the system only needs to be computed once if the plasma parameters, such as electric field strength, effective ion charge, and total particle density, are kept constant [29].

Runaway density

The lower boundary used for the runaway region is p_{sep}, given in equation (3.6). Since the critical momentum is pitch-angle dependent, the runaway density is calculated by integrating over ξ and p:

$$n_{\mathrm{RE}} = 2\pi\int_{-1}^{1}\int_{p_c(\xi)}^{\infty} fp^2\,\mathrm{d}p\,\mathrm{d}\xi = 2\pi\sum_{L=0}^{N_\xi-1}\int_{-1}^{1} P_L(\xi)\int_{p_c(\xi)}^{\infty} f_L(p)p^2\,\mathrm{d}p\,\mathrm{d}\xi. \tag{3.10}$$

Similarly, the runaway current is calculated by

$$j_{\mathrm{RE}} = 2\pi e\int_{-1}^{1}\int_{p_c(\xi)}^{\infty} v\xi fp^2\,\mathrm{d}p\,\mathrm{d}\xi = 2\pi e\sum_{L=0}^{N_\xi-1}\int_{-1}^{1} \xi P_L(\xi)\int_{p_c(\xi)}^{\infty} v\, f_L(p)p^2\,\mathrm{d}p\,\mathrm{d}\xi. \tag{3.11}$$

Self-consistent electric field

A recently added feature in CODE is the ability to calculate the electric field self-consistently with the evolution of the electron distribution. The electric field is induced by the magnetic field created by a runaway beam. The induced field is proportional to the rate of change of the current and given by

$$E = -\frac{L}{2\pi R}\frac{\mathrm{d}I}{\mathrm{d}t} \tag{3.12}$$

$$L \approx \mu_0 R\left(\ln\left(\frac{8R}{a}\right) - 2 + \frac{l_i}{2}\right). \tag{3.13}$$

Here, R and a are the major and minor radii of the tokamak, as indicated in Figure 1.1, and l_i parametrizes the distribution of current within the beam. Equation (3.13) is a good approximation for the inductance L in the case of a large-aspect ratio current loop, such as a runaway beam [45].

3.3 Hot-tail modelling

As discussed in Section 3.1.2, the cooling depends on several phenomena and can generally not be known in advance. We will here describe two different models which have previously been used to model hot-tail generation. The first one, described in Section 3.3.1, uses a prescribed exponential temperature evolution to approximate the electric field evolution and calculate the runaway generation. The second one, described in Section 3.3.2, uses a cooling by radiation model to self-consistently model the temperature drop.

3.3.1 Prescribing temperature evolution

In previous work by H. Smith *et al.* [21, 24], an analytical approximation of the electron distribution function is derived. Focusing on modelling the formation of a possible hot-tail seed, it is assumed that the electric field has a negligible effect on the shape of the distribution, so it remains approximately isotropic. The increased electric field is considered in the model through a change in critical momentum. The temperature evolution is modelled as an exponential decay between the initial and final temperature, where the characteristic time t_{TQ} determines the timescale of the cooling:

$$T(t) = T_{\text{final}} + (T_{\text{initial}} - T_{\text{final}})e^{-t/t_{\mathrm{TQ}}}. \tag{3.14}$$

The kinetic equation (2.9) is used with the collision operator for a background of stationary ions and electrons with a Maxwellian distribution, given in equation (2.35). Neglecting the effect of the electric field takes away the pitch-angle dependence on the left-hand side in the kinetic equation. This removes the pitch-angle scattering term (ν_D) from the collision operator. If the temperature drops rapidly from the pre-cooling temperature T_{initial} to a cold T_{final}, the high-energy tail in the initial distribution gets a velocity much higher than the thermal velocity. In this limit, $v \gg v_T$, the collision operator becomes

$$C(f) = \frac{\nu_{ee0} v_{T0}^3}{v^2} \frac{\partial}{\partial v} \left[\frac{v_T^2}{v^2} \frac{v^2}{v_T^2} f + \frac{v_T^2}{v^2} \frac{v}{2} \frac{\partial f}{\partial v} \right] \approx \frac{\nu_{ee0} v_{T0}^3}{v^2} \frac{\partial f}{\partial v} \tag{3.15}$$

when terms of the order $(v_T/v)^2$ are ignored. Here, ν_{ee0} is the initial thermal collision frequency, see equation (2.39), and $v_{T0} = \sqrt{2T_{\text{initial}}/m_e}$ is the initial thermal velocity for the electrons. The kinetic equation then simplifies to

$$\frac{\partial f}{\partial t} = \frac{\nu_{ee0} v_{T0}^3}{v^2} \frac{\partial f}{\partial v}. \tag{3.16}$$

If the initial distribution is assumed to be a Maxwellian, this has the solution

$$f(t,v) = \frac{n_0}{\pi^{3/2} v_{T0}^3} \exp\left[-\left(\frac{v^3}{v_{T0}^3} + 3\tau(t) \right)^{2/3} \right] \tag{3.17}$$

$$\tau(t) = \nu_{ee0} \int_0^t \frac{n(t')}{n_0} \, \mathrm{d}t'. \tag{3.18}$$

This distribution is isotropic since the influence of the electric field was neglected. The diffusion term that was neglected in equation (3.15) will initially have an influence on the kinetic equation if the temperature follows the assumed exponential cooling in equation (3.14). At early times, equation (3.17) will therefore overestimate the distribution function, necessitating a correction of the time evolution. A good correction of τ was found in [21] to be $\tau(t) = \nu_{ee0}(t - t_*)$ where t_* is a delay time determined by the cooling time scale: $t_* = t_{\mathrm{TQ}}$. This is a good approximation if T_{final} is low, $\lesssim$ 10 eV, but not at higher temperatures such as 100 eV since the diffusion then also influences the distribution at late times. We will verify this in Section 5.3.

Assuming that no electrons escape from the runaway region, meaning that the runaway growth rate remains positive, the hot-tail seed density can be estimated as

$$\begin{aligned} n_{\mathrm{RE}}(t) &= \int_0^{2\pi} \int_{v_c}^{\infty} \int_{\xi_{\mathrm{sep}}(v)}^{1} f(t,v) v^2 \,\mathrm{d}\xi \,\mathrm{d}v \,\mathrm{d}\phi \\ &= 2\pi \int_{v_c}^{\infty} (1 - \xi_{\mathrm{sep}}) v^2 f \,\mathrm{d}v = 4\pi \int_{v_c}^{\infty} (v^2 - v_c^2) f \,\mathrm{d}v. \end{aligned} \tag{3.19}$$

where the critical velocity is $v_c = c\sqrt{E_c/E_\parallel}$ and the separatrix $\xi_{\mathrm{sep}}(v) = 2v_c^2/v^2 - 1$, equivalent to equation (3.6), was used. By applying the change of variables $u^3 = v^3/v_{T0}^3 + 3\tau$ and using the expression (3.17) for f, the runaway seed fraction can be written as

$$\frac{n_{\mathrm{RE}}(t)}{n_0} = \frac{4}{\sqrt{\pi}} \int_{u_c}^{\infty} \left(1 - \frac{(u_c^3 - 3\tau)^{2/3}}{(u^3 - 3\tau)^{2/3}}\right) e^{-u^2} u^2 \,\mathrm{d}u. \tag{3.20}$$

A further simplification is to neglect the effect of the direction of the electric field and count all electrons with $v > v_c$, which in equation (3.19) would correspond to $\xi_{\mathrm{sep}} \equiv -1$. This isotropic runaway region gives the following expression for the runaway fraction:

$$\frac{n_{\mathrm{RE}}(t)}{n_0} = 4\pi \int_{v_c}^{\infty} f(t,v) \,\mathrm{d}v = \frac{2}{\sqrt{\pi}} u_c e^{-u_c^2} + \mathrm{erfc}(u_c), \tag{3.21}$$

where $u_c^3 = v_c^3/v_{T0}^3 + 3\tau$, and erfc denotes the complementary error function. Equations (3.20) and (3.21) should be used as long as the runaway growth rate is positive; when a maximum is reached the runaway density remains at a constant value.

The time evolution of the electric field was approximated by assuming that the total plasma current is constant, and that the current density can be written as $j_\parallel = \sigma_\parallel^{\mathrm{Sp}} E_\parallel$, where $\sigma_\parallel^{\mathrm{Sp}}$ is the parallel Spitzer conductivity which we defined in equation (2.33). This also assumes that the current carried by the runaway population is negligible. Since $\sigma_\parallel^{\mathrm{Sp}}$ is proportional to $T^{3/2}$, current density conservation requires a $T^{-3/2}$ dependence in $E_\parallel$:

$$E_\parallel(t) = E_{\parallel 0} \left(\frac{T_0}{T(t)}\right)^{3/2}, \tag{3.22}$$

where the initial electric field should be chosen to match the current density: $E_{\|0} = j_0/\sigma_{\|}^{\mathrm{Sp}}$. This gives an expression for v_c:

$$v_c = c\sqrt{\frac{E_c}{E_{\|0}}}\left(\frac{T(t)}{T_0}\right)^{3/4}. \tag{3.23}$$

This model for hot-tail generation has been evaluated and compared to CODE simulations on a proof of concept level, with temperatures $T_{\text{initial}} = 3.1$ keV and $T_{\text{final}} = 31$ eV, density $n_0 = 1 \cdot 10^{19}$ m^{-3}, effective charge $Z_{\text{eff}} = 1$ and a cooling time t_{TQ} of 0.3 ms [35]. In this scenario, equation (3.20) underestimated the runaway fraction by an order of magnitude. Equation (3.21) however, which is a more approximate form, comes closer to the value calculated by CODE, only a factor of 2 below. Further investigation of the accuracy of this model for different thermal quench times is shown in Section 5.3.

3.3.2 Self-consistent cooling

Another approach to estimate the distribution function was developed by P. Aleynikov and B.N. Breizman [53]. They viewed a scenario where a cold population with the temperature T_{cold} exists in the plasma from the start and contributes to cooling down the hot population. The cooling is modelled self-consistently assuming that it occurs solely because of radiation.

The kinetic equation for the hot population is written in terms of the normalized relativistic momentum $p = \gamma v/c$ and the pitch-angle θ:

$$\frac{\partial F}{\partial s} + \frac{\partial}{\partial p}\left[E\cos\theta - 1 - \frac{1}{p^2}\right]F = \frac{1}{\sin\theta}\frac{\partial}{\partial\theta}\sin\theta\left[E\frac{\sin\theta}{p}F + \frac{(Z_{\text{eff}}+1)}{2}\frac{\sqrt{p^2+1}}{p^3}\frac{\partial F}{\partial\theta}\right], \tag{3.24}$$

where $F = 2\pi p^2 f$ is the electron momentum distribution function, normalized so that $n_{\text{hot}} = \int F\,\mathrm{d}p\sin\theta\,\mathrm{d}\theta$, s is a time variable defined by $\partial_t s = 1/\tau_c$ where τ_c is the relativistic collision time for the cold bulk given by equation (2.47) and $E = E_{\|}/E_c$ is the ratio between the applied and the critical electric field (see equation (3.3)). In Chapter 4 we will encounter equation (3.24) in another form, equation (4.1). In Appendix A, we show that the two forms are equivalent. The isotropic part of F is found by solving equation (3.24) in the absence of an electric field and with an initial Maxwellian distribution. The solution is the same as in Section 3.3.1, given by equation (3.17) and here expressed as $\bar{F} = F\int\sin\theta\,\mathrm{d}\theta$:

$$\bar{F}(t) = \frac{4cn_{\text{hot}}^0}{\sqrt{\pi}v_{T0}}\frac{v^2}{v_{T0}^2}\exp\left[-\left(\frac{v^3}{v_0^3} + 3\tau(t)\right)^{2/3}\right]. \tag{3.25}$$

The time-dependent τ gives a decay of the hot population through particle flux into the cold bulk. The cold density therefore depends on how many hot electrons have slowed down and the contribution from ionized impurities:

$$n_{\text{cold}}(t) = n_{\text{hot}}^0 - n_{\text{hot}}(t) + n_{\text{imp}}Z_{\text{imp}}(T_{\text{cold}}(t)), \tag{3.26}$$

where n_{imp} is the density of impurity ions and Z_{imp} their average charge state as a function of temperature.

When the electric field is included in the kinetic equation, an anisotropic correction δF_σ can be derived in the high Z_{eff} limit:

$$2E\frac{v^5}{c^2}\cos\theta\frac{\partial}{\partial v}\frac{\bar{F}}{v^2} = \frac{Z_{\text{eff}}}{\sin\theta}\frac{\partial}{\partial\theta}\left[\sin\theta\frac{\partial(\delta F_\sigma)}{\partial\theta}\right]. \tag{3.27}$$

This high Z_{eff} limit is motivated by expecting a high density of impurity ions has been injected into the disrupting plasma. The anisotropic part of the distribution function is used to calculate the fast current, similar to the derivation of the Spitzer conductivity in Section 2.3.2. The total current density changes on a much longer timescale than the thermal quench, and is therefore considered constant $j_{\text{tot}} = j_0$. The total current density from the hot and cold populations is then given by

$$j_0 = \int ev_\parallel \delta F_\sigma \,\mathrm{d}p \sin\theta \,\mathrm{d}\theta + \sigma^{\text{Sp}}_{\parallel\text{cold}} E_\parallel. \tag{3.28}$$

Using the expression (3.27) for δF_σ, this can be written in the form

$$\frac{j_0 - \sigma^{\text{Sp}}_{\parallel\text{cold}} E E_c}{ec} = E\frac{2n_{\text{cold}}}{Z_{\text{eff}} n_{\text{imp}}}\frac{1}{c^4}\int v^3 \bar{F}\,\mathrm{d}v, \tag{3.29}$$

which then can be used to calculate the electric field. In Section 4.1.2 this method to derive the electric field is carried out in detail.

This model of [53] also calculates the temperature evolution self-consistently assuming that radiation is the dominant cooling process. The power-balance equation for the cold electrons is given by

$$\frac{\partial(W_{\text{th}} + W_i(t))}{\partial t} = P_s(F) + \frac{j_c^2}{\sigma_{\text{cold}}} - n_{\text{imp}} n_{\text{cold}} L(T_{\text{cold}}), \tag{3.30}$$

where $W_{\text{th}} = \frac{3}{2} n_{\text{cold}} T_{\text{cold}}$ is the kinetic energy density of the cold electrons, W_i the ionization energy, P_s the stopping power released by the hot population via Coulomb collisions, and $L(T_{\text{cold}})$ is the radiative cooling coefficient for the impurity which depends strongly on temperature [31]. The hot and cold densities vary with time, as well as τ_c due to its n_{cold} dependence. The effective charge Z_{eff}, and therefore σ_{cold}, also changes with time because the impurity charge state is temperature dependent.

Equations (3.24), (3.26), (3.28), and (3.30) were in [53] solved together for $T_{\text{initial}} =$ 4 keV, $n^0_{\text{hot}} = 10^{20}$ m^{-3}, $j_0 = 1$ MA/m^2. Impurities were injected in the form of argon (Ar^{+18}) at different densities between $0.3 \cdot 10^{20}$ and $0.7 \cdot 10^{20}$ m^{-3}. The simulation results show that the hot population density n_{hot} decreases during the thermal quench but then reaches a constant final value. The results show a shorter thermal quench at higher impurity injection, of the order of 0.05 ms for $n_{\text{imp}} = 0.7 \cdot 10^{20}$ m^{-3} and 0.1 ms at $0.4 \cdot 10^{20}$ m^{-3}. The maximum temperature reached by the bulk is also lower at high impurity densities.

In Chapter 4, we will develop a model for hot-tail generation which uses a similar method to calculate the electric field as the one presented here, but with a pre-determined temperature evolution. We then extend the model with a calculation of the runaway density.

4

New models for hot-tail generation

In Section 3.1.1 we saw that slow and fast electrons respond differently to a sudden temperature drop; the slow electrons are cooled down almost instantly while fast electrons take much longer due to their longer collision time. This motivates a division of the electrons into a cold and a hot population with number densities n_{cold} and n_{hot} respectively. Particles move from the hot to the cold population as the hot electrons start to gradually slow down. No electrons are lost from the domain during the thermal quench, so the total density is constant and equal to $n_0 = n_{\mathrm{cold}} + n_{\mathrm{hot}}$.

We will not follow the exact distribution function of the cold population, but only regard it as a cold bulk that can carry ohmic current $j_\Omega = \sigma^{\mathrm{Sp}}_{\|\mathrm{cold}} E_\|$, where $\sigma^{\mathrm{Sp}}_{\|\mathrm{cold}}$ is the Spitzer conductivity, defined in equation (2.33), at T_{final}. The density of cold electrons n_{cold} changes significantly with time, from 0 at $t = 0$ to the majority of n_0 at the end of the cooling. The Spitzer conductivity is however independent of the density except for a weak dependence in the Coulomb logarithm, so it can be assumed constant.

The hot population follows the relativistic kinetic equation that was presented in Section 2.3.4, where the energy-diffusion collision frequency $\nu_\|$ was neglected. We recall that the kinetics are expressed in two-dimensional momentum space parametrized by the normalized momentum $p = \gamma v/c$ and the pitch-angle coordinate $\xi = p_\|/p$:

$$\tau_c \frac{\partial f}{\partial t} + \frac{E_\|}{E_c}\left(\xi \frac{\partial f}{\partial p} + \frac{1-\xi^2}{p}\frac{\partial f}{\partial \xi}\right) = \frac{1}{p^2}\frac{\partial}{\partial p}\left[\bar{\nu}_S \gamma^2 f\right] + \frac{\bar{\nu}_D}{2}\frac{\gamma}{p^3}\frac{\partial}{\partial \xi}\left[(1-\xi^2)\frac{\partial f}{\partial \xi}\right]. \quad (4.1)$$

The collision frequencies appearing are the normalized slowing-down frequency $\bar{\nu}_S$ (equation (2.49)), describing collisional friction, and the normalized deflection frequency $\bar{\nu}_D$ (equation (2.50)), describing scattering which spreads out the distribution function in the pitch-angle. We take the simplified values $\bar{\nu}_S = 1$ and $\bar{\nu}_D = 1 + Z_{\mathrm{eff}}$ for these frequencies throughout this analysis. As discussed in Section 2.3.4, relativistic particles can experience a high effective charge despite the impurity ions having a low ionization degree. We will therefore allow Z_{eff} to range over values higher than would naturally occur in the cold post-thermal quench plasma, to explore the possible impact of screening in a simplified way. The relativistic collision time τ_c is given by equation (2.47), and includes the total electron density n_0. The hot particle density is given by the integral of f over momentum space: $n_{\mathrm{hot}} = 2\pi \int f(p,\xi) p^2 \,\mathrm{d}p\,\mathrm{d}\xi$. In the beginning this is the same as the total density n_0, but as they start to cool down n_{hot} will decrease and the cold bulk density $n_{\mathrm{cold}}(t) = n_0 - n_{\mathrm{hot}}(t)$ increases.

In this chapter we focus on three specific models which allow us to treat the problem of hot-tail generation in a cooling plasma by solving equation (4.1). We will in all three models assume that a high impurity density is present from the start of the thermal quench, and may have been injected to trigger or mitigate a disruption. The first of our models is based on the electric field calculation presented in Section 3.3.2 and extends the model with an explicit calculation of the runaway density. The second is similar to the first, but modifies the runaway region to be consistent with strong pitch-angle scattering. The third is a simplified numerical model which better accounts for the influence of the electric field on the distribution function.

We will model the temperature evolution in the limit of very fast cooling by letting the temperature drop instantly from T_{initial} to T_{final} at $t = 0$. Our models can therefore be seen as upper limits for the runaway density since slower cooling creates fewer runaways, as was discussed in Section 3.1.2. In Chapter 5 we will then benchmark our models against CODE simulation results for different choices of T_{initial}, n_0 and Z_{eff}. We will also compare our models to CODE simulations with different thermal quench times, and determine approximately how long the duration of the thermal quench can be before our models become invalid.

4.1 Analytic model

Here we take an approach to analyzing hot-tail generation inspired by the two previous models described in Sections 3.3.1 and 3.3.2. We will derive an isotropic distribution for the hot population, and a pitch-angle dependent correction which allows a calculation of the fast current. We also explicitly calculate the generated hot-tail seed population.

4.1.1 Distribution functions

Due to the assumed high impurity density, we can expect pitch-angle scattering to be the dominant effect in the kinetic equation. We write the distribution function as the asymptotic expansion $f(t,p,\xi) = f^0 + f^1 + ...$, where $f^0 \gg f^1 \gg ...$ and perform an expansion of equation (4.1) in the large parameter $\bar{\nu}_D/(\tau_c \partial_t f)$. At zeroth order, only the pitch-angle term operates on the distribution, giving

$$\frac{\partial}{\partial \xi}\left[(1-\xi^2)\frac{\partial f^0}{\partial \xi}\right] = 0 \quad \Rightarrow \quad \frac{\partial f^0}{\partial \xi} = 0, \tag{4.2}$$

so $f^0(t,p,\xi) = f^0(t,p)$, that is f^0 is isotropic. For a notation consistent with the Legendre decomposition (3.9) used in CODE, we write the isotropic part of f as f_0, which in this case gives $f^0 = f_0$. To the next order, the other terms are included with f_0, whilst f^1 appears in the last term:

$$\underbrace{\tau_c \frac{\partial f_0}{\partial t}}_{\text{A}} + \underbrace{\frac{E_\parallel}{E_c}\xi\frac{\partial f_0}{\partial p}}_{\text{B}} = \underbrace{\frac{1}{p^2}\frac{\partial}{\partial p}\left[\bar{\nu}_S \gamma^2 f_0\right]}_{\text{C}} + \underbrace{\frac{\bar{\nu}_D}{2}\frac{\gamma}{p^3}\frac{\partial}{\partial \xi}\left[(1-\xi^2)\frac{\partial f^1}{\partial \xi}\right]}_{\text{D}}. \tag{4.3}$$

If we take the zeroth-order moment $\frac{1}{2}\int_{-1}^{1} \mathrm{d}\xi$ of equation (4.3), the contribution of the B term vanishes since it is an odd function integrated over an even interval. The contribution of the D term also vanishes due to the $(1-\xi^2)$ factor:

$$\int_{-1}^{1} \frac{\partial}{\partial \xi}\left[(1-\xi^2)\frac{\partial f^1}{\partial \xi}\right] \mathrm{d}\xi = \left[(1-\xi^2)\frac{\partial f^1}{\partial \xi}\right]_{-1}^{1} = 0. \tag{4.4}$$

The non-zero moments of the remaining terms, A and C, give us the equation for f_0:

$$\tau_c \frac{\partial f_0}{\partial t} = \frac{1}{p^2}\frac{\partial}{\partial p}\left[\bar{\nu}_S \gamma^2 f_0\right]. \tag{4.5}$$

If we define the function $F = \bar{\nu}_S \gamma^2 f_0$, this takes the form

$$\tau_c \frac{\partial F}{\partial t} - \frac{\bar{\nu}_S}{\bar{v}^2}\frac{\partial F}{\partial p} = 0, \tag{4.6}$$

where $\bar{v} = v/c = p/\gamma$ is a normalized velocity. In this model, $\bar{\nu}_S$ is independent of time. Equation (4.6) then has the general solution

$$f_0(t,p) = \frac{1}{\bar{\nu}_S \gamma^2} G\left(s\right), \tag{4.7}$$

$$s(t,p) = \int_0^p \frac{\bar{v}^2}{\bar{\nu}_S}\,\mathrm{d}p + \int_0^t \frac{\mathrm{d}t'}{\tau_c}. \tag{4.8}$$

In our case, the function $G(s)$ must satisfy that the initial distribution $f_0(t=0,p)$ is a Maxwellian,

$$G(s)|_{t=0} = \frac{n}{\pi^{3/2} p_{\mathrm{Te}}^3} \bar{\nu}_S \gamma^2 \exp\left[-p^2/p_{\mathrm{Te}}^2\right], \tag{4.9}$$

where $p_{\mathrm{Te}} = \sqrt{2T_{\mathrm{initial}}/m_e c^2}$ is the initial thermal velocity of the electrons in the plasma, normalized to c.

In the non-relativistic approximation $\gamma = 1 \Rightarrow \bar{v} = p$, and recalling $\bar{\nu}_S = 1$, the first term in s is $p^3/3$. We therefore replace p^2 in equation (4.9) by $(3s)^{2/3}$, giving

$$G(s) = \frac{n}{\pi^{3/2} p_{\mathrm{Te}}^3} \bar{\nu}_S \gamma^2 \exp\left[-(3s)^{2/3}/p_{\mathrm{Te}}^2\right]. \tag{4.10}$$

For $t \neq 0$, $3s = p^3 + 3\int_0^t \mathrm{d}t'/\tau_c$. Consequently, the distribution function takes a form equivalent to (3.17) derived by Smith *et al.* [21]:

$$f_0(t,p) = \frac{n}{\pi^{3/2} p_{\mathrm{Te}}^3} \exp\left[-(p^3 + 3\tau(t))^{2/3}/p_{\mathrm{Te}}^2\right] \tag{4.11}$$

$$\tau(t) = \int_0^t \frac{\mathrm{d}t'}{\tau_c} = \frac{t}{\tau_c}, \tag{4.12}$$

where the final equality holds if τ_c is a constant, as is assumed here since we assume collisions with all electrons and constant total density n_0.

We will now derive an expression for $f^1(t,p,\xi)$. Taking the first order moment $\frac{3}{2}\int_{-1}^{1}\xi\,\mathrm{d}\xi$ of equation (4.3), the A and C integrands are odd and give zero. It is reasonable to take f^1 proportional to ξ [18], since the anisotropic part of the distribution function is expected to be larger in the direction of the electric field, which is where $\xi = 1$. We therefore write $f^1(t,p,\xi) = \xi f_1(t,p)$, again consistent with the Legendre decomposition in CODE. This allows us to evaluate the integrals for B and D:

$$\frac{E_\parallel}{E_c}\frac{\partial f_0}{\partial p} = \frac{3\bar{\nu}_D}{4}\frac{\gamma}{p^3}f_1\int_{-1}^{1}\xi\frac{\partial}{\partial\xi}\left[(1-\xi^2)\right]\mathrm{d}\xi = -\bar{\nu}_D\frac{\gamma}{p^3}f_1. \tag{4.13}$$

This gives an expression for f_1 in terms of f_0:

$$f_1(t,p) = -\frac{1}{\bar{\nu}_D}\frac{p^3}{\gamma}\frac{E_\parallel}{E_c}\frac{\partial f_0(t,p)}{\partial p}. \tag{4.14}$$

Thus, $f(t,p,\xi) = f_0(t,p) + \xi f_1(t,p)$, with equation (4.11) for f_0 and (4.14) for f_1, is a closed expression for the distribution of hot electrons evolving in time under the influence of an electric field in a cooling plasma.

Since $f^1 = \xi f_1$ is odd in the ξ variable, its contribution vanishes when integrating. The hot density is therefore calculated by integrating the isotropic part f_0 of the distribution:

$$n_{\mathrm{hot}}(t) = 4\pi\int f_0(t,p)p^2\,\mathrm{d}p, \tag{4.15}$$

and $n_{\mathrm{cold}}(t) = n_0 - n_{\mathrm{hot}}(t)$. The term -3τ in the exponent of equation (4.11) causes n_{hot} to decrease over time.

4.1.2 Electric field

We will now derive an expression for the electric field, following a scheme inspired by the model described in Section 3.3.2. Since the thermal quench happens on a shorter time scale than the current quench [24, 31], the total current is approximated as constant and equal to its initial value j_0. The fast current j_{fast} is obtained by taking the parallel velocity moment of the electron distribution. Similarly to the derivation of the Spitzer conductivity in a Lorentz gas described in Section 2.3.2, the isotropic part f_0 does not contribute to this odd moment, and only the contribution from f_1 survives:

$$\begin{aligned}
j_{\parallel,\mathrm{fast}} &= e\int v_\parallel f(t,p,\xi)\,\mathrm{d}^3p = e\int v\xi\left(f_0(t,p) + \xi f_1(t,p)\right)p^2\,\mathrm{d}p\,\mathrm{d}\xi\,\mathrm{d}\phi \\
&= e\int_0^{2\pi}\mathrm{d}\phi\int_{-1}^{1}\xi^2\,\mathrm{d}\xi\int_0^\infty vp^2 f_1\,\mathrm{d}p = ec\frac{4\pi}{3}\int_0^\infty\frac{p^3}{\gamma}f_1\,\mathrm{d}p \\
&= -ec\frac{4\pi}{3}\frac{E_\parallel}{E_c}\int_0^\infty\frac{1}{\bar{\nu}_D}\frac{p^6}{\gamma^2}\frac{\partial f_0(t,p)}{\partial p}\,\mathrm{d}p \\
&= -ec\frac{4\pi}{3}\frac{E_\parallel}{E_c}\left(\left[\frac{1}{\bar{\nu}_D}\frac{p^6}{\gamma^2}f_0\right]_0^\infty - \int_0^\infty\frac{\partial}{\partial p}\left[\frac{1}{\bar{\nu}_D}\frac{p^6}{\gamma^2}\right]f_0\,\mathrm{d}p\right) \\
&= \frac{4\pi}{3}\frac{E_\parallel}{E_c}\frac{ec}{1+Z_{\mathrm{eff}}}\int_0^\infty\frac{6p^5+4p^7}{(1+p^2)^2}f_0\,\mathrm{d}p.
\end{aligned} \tag{4.16}$$

We inserted the expression (4.14) for f_1 on the third line and used partial integration to remove the p derivative on the fourth line. The cold population carries an ohmic current $j_\Omega = \sigma^{\mathrm{Sp}}_{\|\mathrm{cold}} E_\|$. We can then write down the current balance

$$j_0 = j_{\|,\Omega} + j_{\|,\mathrm{fast}} = \frac{E_\|}{E_c}\left[\sigma^{\mathrm{Sp}}_{\|\mathrm{cold}} E_c + \frac{4\pi}{3}\frac{ec}{1+Z_{\mathrm{eff}}}\int_0^\infty \frac{6p^5+4p^7}{(1+p^2)^2} f_0 \,\mathrm{d}p\right], \tag{4.17}$$

and so we now have an explicit expression for the self-consistent electric field:

$$E_\|(t) = E_c j_0 \left[\sigma^{\mathrm{Sp}}_{\|\mathrm{cold}} E_c + \frac{4\pi}{3}\frac{ec}{1+Z_{\mathrm{eff}}}\int_0^\infty \frac{6p^5+4p^7}{(1+p^2)^2} f_0(t,p) \,\mathrm{d}p\right]^{-1}. \tag{4.18}$$

This expression will be monotonically increasing, since $f_0(t,p)$ in equation (4.11) decreases with time for all values of p.

The assumption that f is mainly isotropic and that the effect of the electric field only produces a small correction $f_1 \ll f_0$ is only expected to be a good approximation if the electric field is relatively weak. Stronger electric fields contribute to a larger anisotropy in the distribution and thereby also a larger fast current. A correction of the calculation (4.16) would therefore be needed to properly describe the fast current. This, along with better inclusion of the electric field in the distribution function, is explored in the numerical model in Section 4.3.

4.1.3 Runaway generation

The separatrix of the runaway region was defined in equation (3.6) in the limit of no pitch-angle scattering, and should therefore be optimal for low-Z_{eff} situations. Even if we have taken the limit of strong pitch-angle scattering here, we use this definition in this section:

$$p_{\mathrm{sep}}(t) = \sqrt{\frac{E_{\mathrm{c}}}{E_\|(t)}}\sqrt{\frac{2}{1+\xi}}. \tag{4.19}$$

In Section 4.2.2 we will present an improved definition of the runaway region. The runaway density is calculated by integrating over the runaway region $p > p_{\mathrm{sep}}$:

$$n_{\mathrm{RE}} = \int\limits_{p>p_{\mathrm{sep}}} f(t,p,\xi)\,\mathrm{d}^3p. \tag{4.20}$$

Since the critical momentum p_{sep} includes the electric field which evolves in time, the time dependence of the integral limit in equation (4.20) needs to be taken into account. Using Leibniz integral rule, we get

$$\begin{aligned}\frac{\partial n_{\mathrm{RE}}}{\partial t} &= \int_0^{2\pi}\int_{-1}^{1}\frac{\partial}{\partial t}\left[\int_{p_{\mathrm{sep}}(E_\|(t),\xi)}^\infty f(t,p,\xi)p^2\,\mathrm{d}p\right]\mathrm{d}\xi\,\mathrm{d}\phi \\ &= 2\pi\int_{-1}^{1}\left[-f(t,p_{\mathrm{sep}},\xi)p_{\mathrm{sep}}^2\frac{\partial p_{\mathrm{sep}}}{\partial t} + \underbrace{\int_{p_{\mathrm{sep}}}^\infty \frac{\partial}{\partial t}\left[f(t,p,\xi)p^2\right]\mathrm{d}p}_{\text{neglected}}\right]\mathrm{d}\xi \\ &\approx -2\pi\frac{\partial E_\|}{\partial t}\int_{-1}^{1} f_0(t,p_{\mathrm{sep}})p_{\mathrm{sep}}^2(E_\|(t),\xi)\frac{\partial p_{\mathrm{sep}}(E_\|(t),\xi)}{\partial E_\|}\,\mathrm{d}\xi.\end{aligned} \tag{4.21}$$

For convenience we keep only the f_0 contribution in this calculation. Including f_1 is not expected to have a large effect on the growth since $f_1 \ll f_0$, and would only add a small correction to the runaway fraction. In the last step, we have neglected the second term. A physical motivation is that there should be no particle flux through the separatrix for the runaway region if diffusion into the runaway region is neglected; by definition, particles with $p > p_{\text{sep}}$ are accelerated and particles with $p < p_{\text{sep}}$ are decelerated. While this is not formally the case here since we use an approximate expression for p_{sep}, it makes physical sense to omit this term. In Section 4.2 we will present a runaway region more consistent with the strong pitch-angle scattering assumption by defining the critical momentum in a way such that the corresponding term in equation (4.37) vanishes.

With the derivatives

$$\frac{\partial p_{\text{sep}}}{\partial E_\parallel} = -\frac{1}{2}\sqrt{\frac{E_c}{E_\parallel^3}}\sqrt{\frac{2}{1+\xi}} = -\frac{1}{2E_\parallel}p_{\text{sep}} \tag{4.22}$$

$$\frac{\partial \xi}{\partial p_{\text{sep}}} = \frac{\partial}{\partial p_{\text{sep}}}\left[\frac{2E_c}{p_{\text{sep}}^2 E_\parallel} - 1\right] = -\frac{4E_c}{E_\parallel}\frac{1}{p_{\text{sep}}^3}, \tag{4.23}$$

the growth rate is transformed to an integral in p:

$$\begin{aligned}\frac{\partial n_{\text{RE}}}{\partial t} &= -2\pi \frac{\partial E_\parallel}{\partial t}\int_{p_{\text{sep}}|_{\xi=-1}}^{p_{\text{sep}}|_{\xi=1}} p_{\text{sep}}^2 \frac{\partial p_{\text{sep}}}{\partial E_\parallel} f_0(t,p_{\text{sep}})\frac{\partial \xi}{\partial p_{\text{sep}}}\,\mathrm{d}p_{\text{sep}} \\ &= 4\pi \frac{E_c}{E_\parallel^2}\frac{\partial E_\parallel}{\partial t}\int_{\sqrt{E_c/E_\parallel}}^{\infty} f_0(t,p)\,\mathrm{d}p.\end{aligned} \tag{4.24}$$

This expression, with the electric field given by equation (4.18) and the distribution function in equation (4.11), completes the first, analytic, model we will use to calculate the runaway growth rate, denoted “analytic, p_{sep}”. The growth rate will always be positive since $E_\parallel$ is monotonically increasing in this model.

4.2 Analytic model, alternative runaway region

To further develop the analytical model derived in Section 4.1 we now derive a new definition for the runaway region that is consistent with our assumed limit of strong pitch-angle scattering. For this we use an ordering of the terms in the kinetic equation inspired by the approach in [20, 33], where the kinetic equation was solved to derive the avalanche growth rate in a scenario with strong pitch-angle scattering but where the electric field is larger the critical field.

4.2.1 Distribution functions

We will solve the same equation (4.1) as in the first model in the limit of strong pitch-angle scattering, but this time also assume that the electric field is stronger than the critical electric field: $\bar{\nu}_D\gamma/p^3 \gg E_\parallel/E_c \gg 1$. This assumption is valid for high Z_{eff} and when the electric field has a non-negligible effect on the distribution function. As before, the time derivative of the distribution function and the friction term are assumed small: $\tau_c\partial_t f \sim \bar{\nu}_S\gamma^2/p^3 \ll E_\parallel/E_c$. The ordering is expressed in the small variable $\delta \sim E_c/E_\parallel$, and we set

$$\underbrace{\tau_c\frac{\partial f}{\partial t}}_{\mathcal{O}(\delta^0)} + \underbrace{\frac{E_\parallel}{E_c}\left(\xi\frac{\partial f}{\partial p} + \frac{1-\xi^2}{p}\frac{\partial f}{\partial \xi}\right)}_{\mathcal{O}(\delta^{-1})} = \underbrace{\frac{1}{p^2}\frac{\partial}{\partial p}\left[\bar{\nu}_S\gamma^2 f\right]}_{\mathcal{O}(\delta^0)} + \underbrace{\frac{\bar{\nu}_D}{2}\frac{\gamma}{p^3}\frac{\partial}{\partial \xi}\left[(1-\xi^2)\frac{\partial f}{\partial \xi}\right]}_{\mathcal{O}(\delta^{-2})}. \quad (4.25)$$

As in Section 4.1, the pitch-angle scattering term is dominant ($\mathcal{O}(\delta^{-2})$), which makes the distribution function isotropic to the zeroth order: $\partial_\xi f^0 = 0$ or $f^0(t,p,\xi) = f^0(t,p) \equiv f_0(t,p)$. Now, at first order, $\mathcal{O}(\delta^{-1})$, the electric field acceleration competes with pitch-angle scattering, and inserting the isotropic form of f^0 we have

$$\frac{E_\parallel}{E_c}\xi\frac{\partial f_0}{\partial p} = \frac{\bar{\nu}_D}{2}\frac{\gamma}{p^3}\frac{\partial}{\partial \xi}\left[(1-\xi^2)\frac{\partial f^1}{\partial \xi}\right]. \quad (4.26)$$

Integrating over $\int_{-1}^{\xi} d\xi'$ allows us to express f^1 in terms of f_0:

$$\frac{1}{2}\frac{E_\parallel}{E_c}\frac{\partial f_0}{\partial p}(\xi^2-1) = \frac{\bar{\nu}_D}{2}\frac{\gamma}{p^3}(1-\xi^2)\frac{\partial f^1}{\partial \xi} \quad (4.27)$$

$$\frac{\partial f^1}{\partial \xi} = -\frac{1}{\bar{\nu}_D}\frac{p^3}{\gamma}\frac{E_\parallel}{E_c}\frac{\partial f_0}{\partial p} \quad (4.28)$$

$$\Rightarrow \quad f^1(t,p,\xi) = -\frac{1}{\bar{\nu}_D}\frac{p^3}{\gamma}\frac{E_\parallel}{E_c}\frac{\partial f_0(t,p)}{\partial p}\xi = \xi f_1(t,p). \quad (4.29)$$

Thus we find the same result for f^1 as obtained with the previous model (equation (4.14)), but here no assumption was made beforehand about the ξ dependence. Finally the second order, $\mathcal{O}(\delta^0)$, is considered. Now the time derivative and friction terms enter the picture:

$$\tau_c\frac{\partial f_0}{\partial t} + \frac{E_\parallel}{E_c}\left(\xi\frac{\partial f^1}{\partial p} + \frac{1-\xi^2}{p}\frac{\partial f^1}{\partial \xi}\right) = \frac{1}{p^2}\frac{\partial}{\partial p}\left[\bar{\nu}_S\gamma^2 f_0\right] + \frac{\bar{\nu}_D}{2}\frac{\gamma}{p^3}\frac{\partial}{\partial \xi}\left[(1-\xi^2)\frac{\partial f^2}{\partial \xi}\right] \quad (4.30)$$

Integrating over $\frac{1}{2}\int_{-1}^{1} \mathrm{d}\xi$, the last term vanishes as in equation (4.4) in the first model, while the second term gives

$$\begin{aligned}\frac{1}{2}\int_{-1}^{1}\frac{E_\parallel}{E_c}\left(\xi\frac{\partial f^1}{\partial p} + \frac{1-\xi^2}{p}\frac{\partial f^1}{\partial \xi}\right)\mathrm{d}\xi &= \frac{1}{2}\int_{-1}^{1}\frac{E_\parallel}{E_c}\left(\frac{1}{p^2}\frac{\partial}{\partial p}\left[\xi p^2 f^1\right] + \frac{\partial}{\partial \xi}\left[\frac{1-\xi^2}{p}f^1\right]\right)\mathrm{d}\xi \\ &= \frac{1}{2}\frac{E_\parallel}{E_c}\frac{1}{p^2}\frac{\partial}{\partial p}\left[\int_{-1}^{1}p^2\xi f^1\,\mathrm{d}\xi\right] \\ &= -\frac{1}{2}\left(\frac{E_\parallel}{E_c}\right)^2\frac{1}{p^2}\frac{\partial}{\partial p}\left[\frac{1}{\bar{\nu}_D}\frac{p^5}{\gamma}\frac{\partial f_0}{\partial p}\int_{-1}^{1}\xi^2\,\mathrm{d}\xi\right] \\ &= -\frac{1}{3}\left(\frac{E_\parallel}{E_c}\right)^2\frac{1}{p^2}\frac{\partial}{\partial p}\left[\frac{1}{\bar{\nu}_D}\frac{p^5}{\gamma}\frac{\partial f_0}{\partial p}\right],\end{aligned} \quad (4.31)$$

where equation (A.3) in Appendix A was used in the first equality. We now get the following equation for f_0, which includes the effect of the electric field:

$$\tau_c \frac{\partial f_0}{\partial t} - \frac{1}{p^2}\frac{\partial}{\partial p}\left[\frac{1}{3}\left(\frac{E_\|}{E_c}\right)^2 \frac{1}{\bar{\nu}_D}\frac{p^5}{\gamma}\frac{\partial f_0}{\partial p} + \bar{\nu}_S \gamma^2 f_0\right] = 0. \tag{4.32}$$

For weak electric fields, and for small p values, this reduces to the same equation as in the first model (4.5) which we found had an explicit analytic solution (4.11). While equation (4.32) is a more general equation for f_0, no analytic solution is available and it needs to be solved numerically. In the current model, we therefore choose to simplify the analysis by keeping the analytic expression (4.11) for f_0, as well as equation (4.18) for the electric field.

Equation (4.32) is used in this model only to derive a correction to the lower boundary of the runaway region, as we will see in Section 4.2.2. In our last model, described in the next section, we will solve the full equation (4.32) numerically.

4.2.2 Critical momentum and runaway generation

Here we use the extended result (4.32) to derive a definition for the critical momentum, referred to as p_c, which is consistent with strong pitch-angle scattering. We note that equation (4.32) can be rewritten in divergence form:

$$\frac{\partial f_0}{\partial t} = \boldsymbol{\nabla}\cdot\mathbf{S} = \frac{1}{p^2}\frac{\partial}{\partial p}\left[p^2 S\right] \tag{4.33}$$

$$S = \underbrace{\frac{1}{3}\left(\frac{E_\|}{E_c}\right)^2 \frac{1}{\tau_c\bar{\nu}_D}\frac{p^3}{\gamma}\frac{\partial f_0}{\partial p}}_{\text{spreads out the distribution}} + \underbrace{\frac{\bar{\nu}_S}{\tau_c}\frac{\gamma^2}{p^2}f_0}_{\text{slows down}} \equiv D\frac{\partial f_0}{\partial p} + A f_0. \tag{4.34}$$

In equation (4.33), $\boldsymbol{\nabla}\cdot\mathbf{S}$ denotes the divergence of the vector $\mathbf{S} = S(p)\hat{p}$ in spherical coordinates. Since $\mathbf{S}$ has no angular dependence as f_0 is isotropic, it can be interpreted as a flux vector in the radial direction in momentum space. Note that a *positive* $S(p_0)$ stands for a net flow of particles *into* the sphere $p < p_0$. The first term in (4.34) is negative since $\partial_p f_0 < 0$ for all p, and acts as an isotropic acceleration of the particles which spreads f_0 in the p direction. The second term is always positive and acts as a friction term which slows down the particles. For small p values the second, slowing-down term is dominant, but for larger p the first term takes over and the particles are accelerated. The runaway region is therefore defined by the critical momentum for which the two terms balance each other:

$$p_c: \qquad D\frac{\partial f_0}{\partial p} + A f_0\bigg|_{p=p_c} = 0. \tag{4.35}$$

Particles with $p < p_c$ are slowed down by the friction term, while particles with $p > p_c$ are accelerated to relativistic speeds by the electric field and run away. The runaway region is isotropic, and we can calculate the runaway density by integrating over $p > p_c$. Again, note that the time dependence of p_c needs to be accounted for when taking the derivative:

$$n_{\mathrm{RE}} = 4\pi \int_{p_c(t)}^{\infty} p^2 f_0(t,p)\,\mathrm{d}p \tag{4.36}$$

$$\frac{\partial n_{\mathrm{RE}}}{\partial t} = -4\pi p_c^2 \frac{\partial p_c}{\partial t} f_0(t,p_c) + 4\pi \int_{p_c}^{\infty} p^2 \frac{\partial f_0}{\partial t}\,\mathrm{d}p. \tag{4.37}$$

The last term is calculated using equation (4.33) for $\partial_t f_0$:

$$\begin{aligned}
4\pi \int_{p_c}^{\infty} p^2 \frac{\partial f_0}{\partial t}\,\mathrm{d}p &= 4\pi \int_{p_c}^{\infty} \frac{\partial}{\partial p}\left[p^2\left(D\frac{\partial f_0}{\partial p} + Af_0\right)\right]\mathrm{d}p \\
&= 4\pi \left[p^2\left(D\frac{\partial f_0}{\partial p} + Af_0\right)\right]_{p=p_c}^{\infty} \\
&= -4\pi p_c^2 \left(D\frac{\partial f_0}{\partial p} + Af_0\right)\Bigg|_{p=p_c} = 0
\end{aligned} \tag{4.38}$$

where the last step follows directly from the definition of p_c in equation (4.35). The runaway growth rate can therefore be expressed as

$$\frac{\partial n_{\mathrm{RE}}}{\partial t} = -4\pi p_c^2 \frac{\partial p_c}{\partial t} f_0(t,p_c). \tag{4.39}$$

For the time evolution of f_0, we recall that the electric field term in the kinetic equation (4.32) was neglected. Since this term is proportional to p^5, its effect decreases rapidly with decreasing p. For low p values, this is therefore a good approximation. At larger p, more precisely for $p > p_c$, the electric field acceleration will dominate, which contradicts our initial assumption of dominant pitch-angle scattering. The reason that equation (4.39) can still provide a valid approximation is that f_0 is evaluated at the point p_c, and the critical momentum decreases with time as the electric field increases. Therefore, when some point p_0 on the p axis is equal to p_c at the time t_0, it has during the time $t < t_0$ been in the region $p < p_c$, where the electric field term has a small effect on the distribution function compared to the slowing-down term. Then $f_0(t < t_0,p_0)$ is well approximated by the analytic expression (4.11), and provided that the distribution function does not change very quickly with time, this also holds for $f_0(t,p_c)$. Thus we motivate our use of equations (4.39), (4.11), and (4.35) to define the runaway growth rate in our second model, denoted "analytic, alt. p_c".

4.3 Simplified numerical model

In this third model model we will use a numerical solution of equation (4.32) to determine f_0 and form a more complete growth rate model. The electric field and the distribution function now depend on each other and the solution must be obtained by numerical iteration. In addition, the fast current is calculated more accurately by dividing the momentum axis into regions and improving the treatment of the runaway current.

4.3.1 Kinetic equation

In this model, the electric field is included in the calculation of f_0. The reduced kinetic equation used is that given in equation (4.33):

$$\frac{\partial f_0}{\partial t} = \boldsymbol{\nabla} \cdot \mathbf{S} = \frac{1}{p^2}\frac{\partial}{\partial p}\left[p^2 S\right] \tag{4.40}$$

$$S(t,p) = \frac{1}{3}\left(\frac{E_\parallel(t)}{E_c}\right)^2 \frac{1}{\tau_c \bar{\nu}_D}\frac{p^3}{\gamma}\frac{\partial f_0(t,p)}{\partial p} + \frac{\bar{\nu}_S}{\tau_c}\frac{\gamma^2}{p^2} f_0(t,p). \tag{4.41}$$

The kinetic equation here is written in divergence form which allows us to interpret $S(t,p)$ as the flux at the time t of particles into a sphere in momentum space with radius p. The total flow rate across the surface of the sphere is $F_p(t,p) \equiv 4\pi p^2 S(t,p)$.

4.3.2 Current density calculation

The models described in Sections 4.1 and 4.2 do not properly include the current carried by the runaway population which has escaped from the distribution. The reason for this is that our initial assumption $\bar{\nu}_D\gamma/p^3 \gg E_\parallel/E_c$ breaks down for large p values, where instead the electric field acceleration should have the largest effect on the electron trajectories. The analytic distribution functions presented will therefore not capture the fastest particles correctly. As part of the model here, we introduce an improved description of the current carried by the faster particles. Additionally, the current carried by the runaway population is added separately to the current balance, which should overall give a more accurate calculation of the electric field.

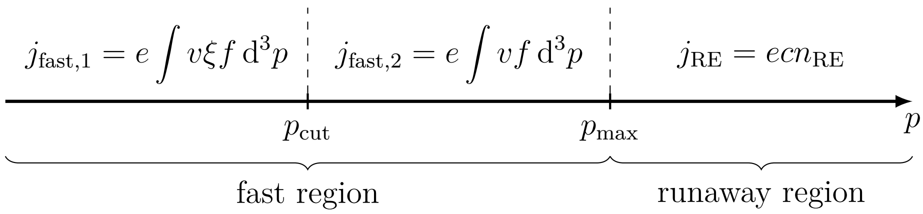

Figure 4.1: Momentum regions in the simplified numerical model.

Instead of the current calculation presented in section 4.1.2, the momentum axis is now divided into three regions. The runaway region contains the particles with $p > p_{\max}$, where $p_{\max}$ is of the order of $m_e c$. In the runaway region, we assume that all particles travel in the forward direction, i.e. $\xi = 1$, and have the velocity $v = c$. The number of particles in the runaway region, n_{RE}, is decided by the particle flow past the momentum limit $p_{\max}$,

$$\frac{\partial n_{\text{RE}}}{\partial t} = -F_p(t,p_{\max}) \tag{4.42}$$

$$j_{\text{RE}} = ecn_{\text{RE}} = -ec\int_0^t F_p(t,p_{\max})\,\mathrm{d}t. \tag{4.43}$$

In the lower part of the fast region, for particles with $p < p_{\text{cut}}$, the current is calculated by taking the parallel velocity moment of the distribution function, as was done in equation (4.16):

$$j_{\text{fast},1} = e \int\limits_{p<p_{\text{cut}}} v\xi f(t,p,\xi)\,\mathrm{d}^3p = -ec\frac{4\pi}{3}\frac{E_\parallel}{E_c}\int_0^{p_{\text{cut}}} \frac{1}{\bar{\nu}_D}\frac{p^6}{\gamma^2}\frac{\partial f_0}{\partial p}\,\mathrm{d}p. \tag{4.44}$$

The current in the upper part of the fast region is corrected by letting all particles travel with $\xi = 1$, while assuming that the time evolution of the distribution function is relatively accurate,

$$\begin{aligned} j_{\text{fast},2} &= e \int\limits_{p_{\text{cut}}<p<p_{\max}} v f(t,p,\xi)\,\mathrm{d}^3p = e\int v\left(f_0(t,p) + \xi f_1(t,p)\right)p^2\,\mathrm{d}p\,\mathrm{d}\xi\,\mathrm{d}\phi \\ &= e\int_0^{2\pi}\mathrm{d}\phi\int_{-1}^{1}\mathrm{d}\xi\int_{p_{\text{cut}}}^{p_{\max}} vp^2 f_0\,\mathrm{d}p = ec4\pi\int_{p_{\text{cut}}}^{p_{\max}}\frac{p^3}{\gamma}f_0\,\mathrm{d}p. \end{aligned} \tag{4.45}$$

To get a smooth transition between the regions, p_{cut} is defined as the momentum at which $j_{\text{fast},1}$ and $j_{\text{fast},2}$ are equal:

$$e2\pi\int_{-1}^{1} v\xi f\,\mathrm{d}\xi = e2\pi\int_{-1}^{1} vf\,\mathrm{d}\xi \tag{4.46}$$

$$\Leftrightarrow \quad \int_{-1}^{1}\xi^2\,\mathrm{d}\xi f_1 = \int_{-1}^{1}\mathrm{d}\xi f_0 \tag{4.47}$$

$$\Leftrightarrow \quad -\frac{1}{3}\frac{1}{\bar{\nu}_D}\frac{p^3}{\gamma}\frac{E_\parallel}{E_c}\frac{\partial f_0}{\partial p} + f_0 = 0 \quad \text{at } p = p_{\text{cut}}. \tag{4.48}$$

For weak electric fields, $p_{\text{cut}} > p_{\max}$. In this case the momentum axis only consists of two regions where $j_{\text{fast},1}$ (4.44) is used for $p < p_{\max}$ and j_{RE} (4.43) is used for $p > p_{\max}$. The fast particle population n_{fast}, is defined as

$$n_{\text{fast}} = \int\limits_{p<p_{\max}} f\,\mathrm{d}^3p = 4\pi\int_0^{p_{\max}} f_0(t,p)p^2\,\mathrm{d}p, \tag{4.49}$$

and the total hot particle density is defined as the sum

$$n_{\text{hot}} = n_{\text{fast}} + n_{\text{RE}}. \tag{4.50}$$

As in the other models, the kinetic equation only models the hot population. We must therefore add an ohmic current $j_\Omega = \sigma^{\text{Sp}}_{\parallel\text{cold}}E_\parallel$ to the current balance, still assuming constant current $j_{\text{tot}} = j_0$ and with the cold particle density given by $n_{\text{cold}} = n_0 - n_{\text{hot}}$. Thus,

$$\begin{aligned} j_{\text{tot}} =& j_0 = j_\Omega + j_{\text{fast},1} + j_{\text{fast},2} + j_{\text{RE}} \\ =& E_\parallel\sigma - ec\frac{4\pi}{3}\frac{E_\parallel}{E_c}\int_0^{p_{\text{cut}}}\frac{1}{\bar{\nu}_D}\frac{p^6}{\gamma^2}\frac{\partial f_0}{\partial p}\,\mathrm{d}p \\ &+ ec4\pi\int_{p_{\text{cut}}}^{p_{\max}}\frac{p^3}{\gamma}f_0\,\mathrm{d}p - ec\int_0^t F_p(t,p_{\max})\,\mathrm{d}t, \end{aligned} \tag{4.51}$$

and the expression for the self-consistent electric field in this model, denoted "numerical", is given by

$$E_{\parallel} = E_c \frac{j_0 - ec4\pi \displaystyle\int_{p_{\text{cut}}}^{p_{\max}} \frac{p^3}{\gamma} f_0 \,\mathrm{d}p + ec \int_0^t F_p(t,p_{\max}) \,\mathrm{d}t}{E_c\sigma - ec\dfrac{4\pi}{3} \displaystyle\int_0^{p_{\text{cut}}} \frac{1}{\bar{\nu}_D} \frac{p^6}{\gamma^2} \frac{\partial f_0}{\partial p} \,\mathrm{d}p}. \tag{4.52}$$

At $t = 0$, no particles have moved out of the distribution through $p_{\max}$ and none of the particles have slowed down into the cold population, which means that $n_{\mathrm{RE}} = n_{\text{cold}} = 0$ and $n_{\text{hot}} = n_0$. As $t \to \infty$, all particles have either slowed down or run away, which means that $n_{\text{hot}} = n_{\mathrm{RE}}$ and the hot current is carried entirely by n_{RE}.

Note that the details of the runaway region are ignored in this analysis. The runaway population is simply defined as all particles with $p > p_{\max}$, a constant value that, unlike p_{sep} and p_c used in the analytic models in Sections 4.1 and 4.2, is independent of the electric field. The numerical calculation of n_{RE} will therefore not resemble simulation results at early points in time, but it will give a good estimate for the final value of n_{RE} if the distribution function is well described by equation (4.40). It has been found in previous work [35] that the exact critical momentum used becomes less important when a large tail of hot electrons has formed. In Appendix B we show an example of this.

In Chapter 5, this model together with the analytical models from Sections 4.1 and 4.2 are benchmarked against CODE simulation results when T_{initial}, n_0 and Z_{eff} are varied. We will find that the first analytic model is our best alternative when $Z_{\text{eff}} = 1$, and that the numerical model works best for high Z_{eff}.

5
Comparing with simulations

In this chapter we will investigate the runaway populations produced by the models that were developed in Chapter 4 and, in a series of parameter scans, compare them to the results of simulation with CODE, which was described in Section 3.2. We recall that CODE is our most exact tool to model the electron distribution function and runaway generation under chosen conditions. The CODE results are therefore taken as the "true" values which our new models aspire to meet.

We remind the reader that in our models we consider an initial plasma with a Maxwellian distribution (see equation (2.12)), and a temperature T_{initial}. To model a very fast cooling, the temperature is dropped to T_{final} at $t = 0$. If we recall from Section 3.1.2 that the runaway generation increases for faster cooling, we can see the result for a sudden temperature drop as an upper limit for the predicted hot-tail seed. The total electron density n_0 is assumed to be constant. We take the initial current density to be $j_0 = 1$ MA/m^2, which is close to the value expected at the magnetic axis in ITER [8]. We first illustrate how the runaway density calculated by the models evolves in time towards a final value and how these compare to the simulation results from CODE. We then perform a parameter study, where we find that the analytic model ("analytic, p_{sep}") from Section 4.1, which used a pitch-angle dependent runaway region, best follows the CODE results in cases with a low effective ion charge $Z_{\mathrm{eff}} = 1$. For a high effective charge, the numerical model ("numerical") from Section 4.3 works best as compared to the other models. We will therefore mainly focus on comparing the models "analytic, p_{sep}" and "numerical". The analytic model "analytic, alt. p_c" from Section 4.2, which uses an alternative runaway region adapted for strong pitch-angle scattering, is included for comparison.

Finally we consider the impact of the assumed cooling time. We observe that the assumption of an exponential temperature decay described in Section 3.3.1 captures the hot-tail generation during slow cooling, but breaks down for cooling times below a few thermal collision times. For such rapid cooling, we can instead accurately describe the hot-tail generation with our models developed in Chapter 4.

5.1 Distribution functions

In this section we present the time evolution of the rapidly cooled electron distribution function and the runaway population for a typical set of disruption parameters. Recall from Section 2.3.4 that fast electrons can experience a high effective charge despite a low ionization degree of impurities at post thermal quench temperatures. Here we therefore take the limit of very high effective charge, $Z_{\text{eff}} = 20$, to explore the effects of strong pitch-angle scattering.

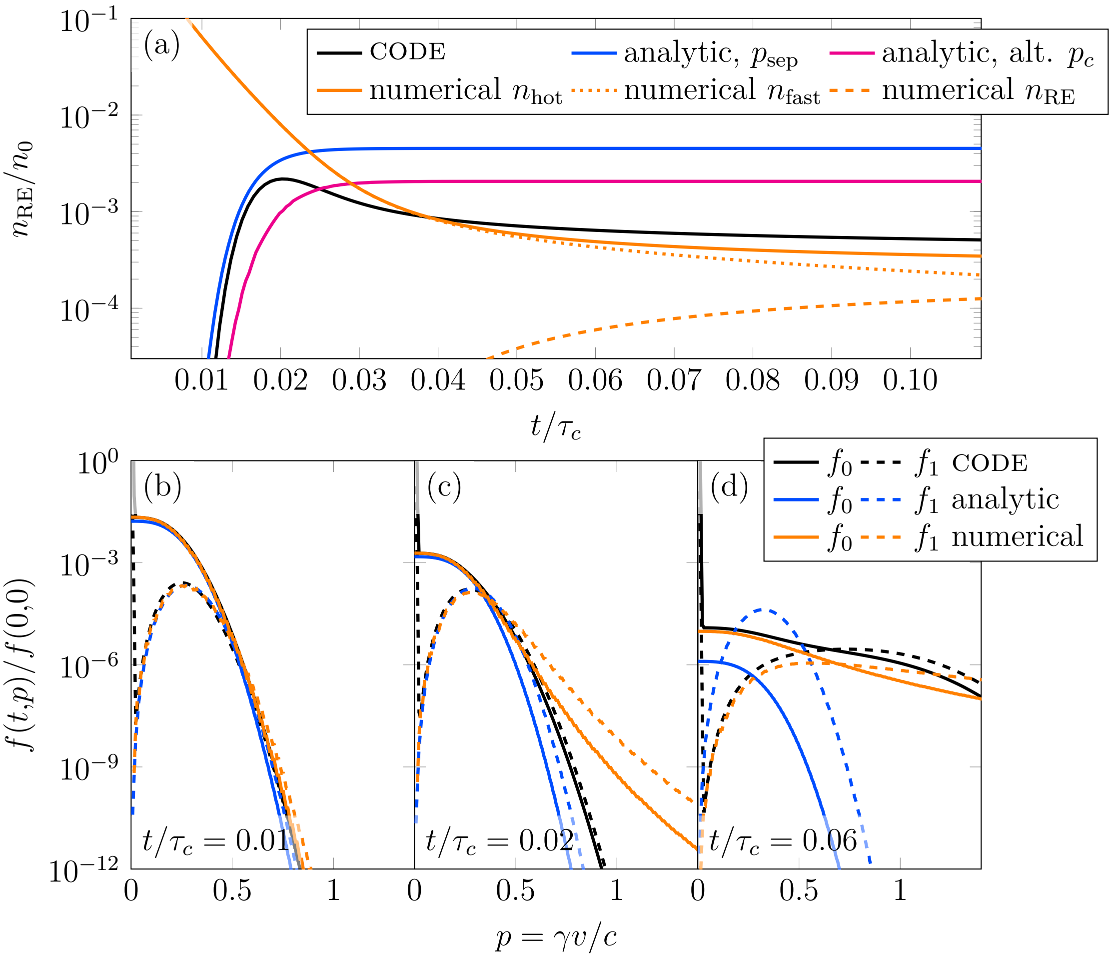

Figure 5.1: Figure (a) shows a typical time evolution of the runaway fraction calculated by CODE (black), the analytic models of Section 4.1 (blue) and Section 4.2 (pink) and the numerical model of Section 4.3 (orange). The parameters used were $T_{\text{initial}} = 6$ keV, $T_{\text{final}} = 5$ eV, $Z_{\text{eff}} = 20$, and $n_0 = 10^{20}$ m^{-3}. The time axis is normalized to the relativistic collision time τ_c (equation (2.47)), which in this case was 34.8 ms. The distribution functions f_0 (solid) and f_1 (dashed) are displayed in Figure (b)-(d) at three different times: $t/\tau_c = 0.01$, 0.02 and 0.06.

We focus on comparing the evolution obtained with CODE, described in Section 3.2, using a self-consistent calculation of the electric field and a pitch-angle dependent runaway region, as described in Section 3.2, to that produced by the analytic model "analytic, p_{sep}" of Section 4.1 and the numerical solution of the model given in Section 4.3. Figure 5.1(a) shows the evolution of the runaway fraction, with the black curve the numerical CODE calculation. The blue curve shows the analytic model. The second analytic model which uses an alternative, isotropic runaway region ("analytic, alt. p_c") described in Section 4.2 is represented by the pink curve in the figure. Both analytic models approximately capture the shape of the CODE curve – they initially have similar slopes and reach their maximum values at similar points in time, around $0.02 - 0.03\tau_c$. What the analytic models do not capture is the decrease of n_{RE} that CODE shows before stabilising at a value almost ten times below its maximum. This overshoot shows that some fast electrons are counted as runaways by our definition of the runaway region, but are slowed down back into the thermal distribution. In other words, the separatrix (equation (3.5)) used in CODE is approximate. However, since the details of the lower boundary become unimportant when the tail in the distribution is large (and modelled correctly) [35], the final value of the runaway fraction is insensitive to the details of the separatrix.

The orange curves were obtained using an implementation of the numerical model in Section 4.3. The solid curve shows the hot density (equation (4.50)), defined as the sum of the fast (n_{fast}, dotted) and runaway (n_{RE}, dashed) densities. The numerical curve is initially very different from the others, due to the definition of the hot population which in this model equals the total electron population when $t = 0$. After a short time, however, we see that the numerical curve follows the decrease in the CODE curve and stabilizes at a value just below the CODE result.

In Figures 5.1(b)-(d), the corresponding electron distribution functions from each model are compared at three different times during the runaway generation. Figure 5.1(b) shows a point before any significant runaway generation. The zeroth and first Legendre modes of the CODE distributions, corresponding to the $f_0(t,p)$ and $f_1(t,p)$ in the analytic models, are shown as black solid and dashed lines respectively. These also include the cold electrons, which show up as thin, almost invisible, peaks around $p = 0$. Since the analytic (blue) and numerical (orange) distributions only describe the hot population, they do not show this peak. In Figure 5.1(c), we show the point $t/\tau_c = 0.02$ where the CODE runaway fraction in Figure 5.1(a) reaches its maximum. Here the CODE and analytic distributions have similar shapes, which is consistent with the similarity between the blue and black curves for $t/\tau_c < 0.02$ in Figure 5.1(a). Finally, in Figure 5.1(d), the electric field has had time to accelerate the distribution and pull out a tail in f_0 and f_1. Here, our analytic model breaks down since the electric field is neglected in f_0. However, the numerical model, where f_0 is calculated with the influence of a self-consistent electric field, follows the CODE distributions well in both f_0 and f_1.

5.2 Parametric dependencies

We will now consider how variation of the controlling parameters affects the runaway evolution, and the ability of our models to capture this behaviour. We will compare two cases with low and high effective ion charge, specifically $Z_{\mathrm{eff}} = 1$ and $Z_{\mathrm{eff}} = 20$. In both cases, we look at the effect of the pre-cooling plasma temperature T_{initial} and also how our models perform at different electron densities n_0.

We take two limits for the effective ion charge. The limit $Z_{\mathrm{eff}} = 1$ is a pure plasma with only hydrogen ions present, corresponding to an unmitigated disruption or mitigation by deuterium injection. The $Z_{\text{eff}} = 20$ limit represents a high density of highly charged impurities. Again, note that we use a higher Z_{eff} than would be expected at cold post thermal quench temperatures, to mock up screening effects on fast particles. When studying the dependence on the initial plasma temperature, we scanned values between 2 and 20 keV – a range covering the initial temperatures of current machines through to reactor scale devices. A relatively high final temperature was used in the first two parameter scans (Sections 5.2.1 and 5.2.2) in order to test the sensitivity of our models when the runaway conversion is low. The range of densities used in Section 5.2.3 was chosen to compare the runaway fractions calculated by our models in cases of both high and low conversion.

5.2.1 Initial temperature, low effective ion charge

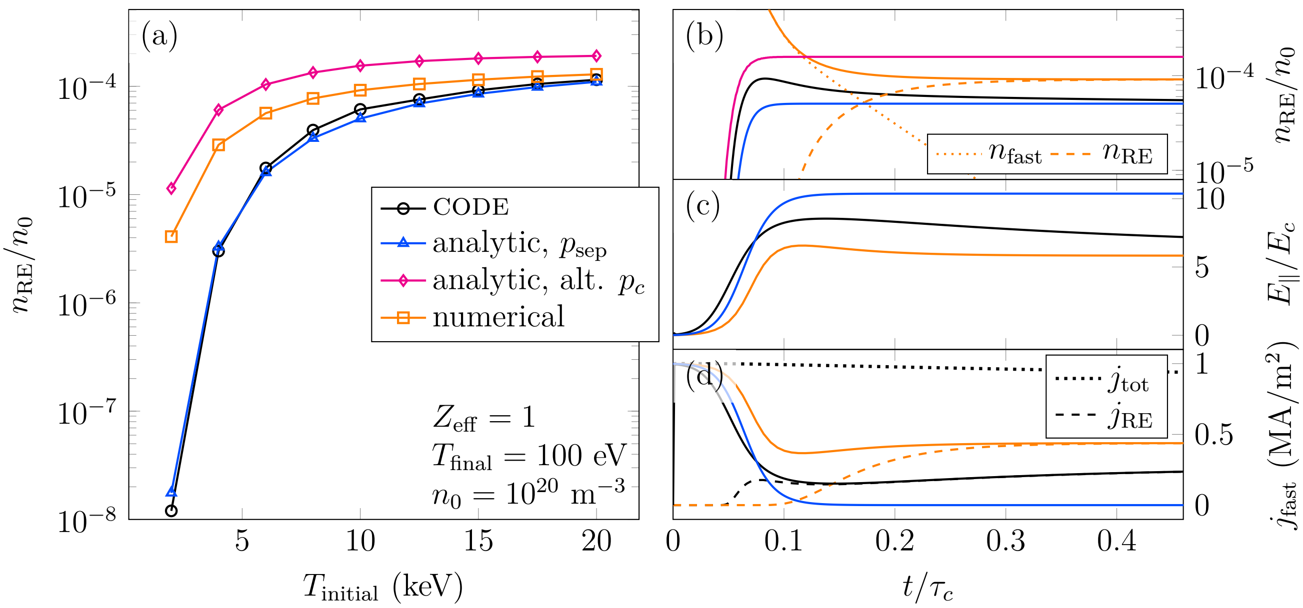

Figure 5.2: Figure (a) shows the runaway fraction obtained by CODE (black), our analytic models (blue, pink) and numerical model (orange), as a function of the pre-cooling temperature, T_{initial}. The parameters used were $Z_{\text{eff}} = 1$, $T_{\text{final}} = 100$ eV and $n_0 = 10^{20}$ m^{-3}. Figure (a) shows the final values when the pre-cooling temperature was varied. Figure (b)-(d) show the time evolution of the runaway fraction, electric field and fast current when $T_{\text{initial}} = 10$ keV.

We first consider the pure plasma situation where the effective ion charge Z_{eff} is 1. In Figure 5.2(a), we have scanned values of T_{initial} ranging from 2 to 20 keV. We kept T_{final} constant at 100 eV and the density was 10^{20} m^{-3}. The final runaway fractions calculated by the different models are shown. The analytic model "analytic, p_{sep}" from Section 4.1 is consistently closer to the CODE result, with a relative error less than 1.2. This is expected since it uses a separatrix p_{sep} that works best when $Z_{\text{eff}} = 1$.

In Figures 5.2(b)-(c) the evolution of the runaway fraction, electric field and fast current density are shown for the different models for the case when T_{initial} was 10 keV. The runaway fractions in Figure 5.2(b) are calculated in the same way as in Figure 5.1(a), and we see again that the the final value of n_{RE} is best approximated by the model "analytic, p_{sep}" (blue). The electric fields and the fast current densities are presented in Figure 5.2(c)-(d). The curves mirror each other since the electric field is proportional to $j_0 - j_{\text{fast}}$. The analytic models use the same expression for the electric field and fast current; the blue curve therefore represents both models. We can see here that the analytic model overestimates the electric field. The main reason for this is that the analytic models do not properly include the current carried by the runaway population, and thereby underestimate the total fast current. The dashed black and orange curves show the part of the fast current made up by runaways in CODE (equation (3.10)) and the numeric model (equation (4.43)). At the end of the process shown, we see that the fast current consists entirely of runaways, and that the fast current from the analytical model dies out as the hot population slows down. Recall that our analytic and numerical models assume the total current density to be constant during the thermal quench. This was checked by plotting the total current density calculated by CODE (black, dotted). During the first $0.2\tau_c$, where most of the runaway generation occurs, j_{tot} decreases by 2 %. We consider this variation sufficiently small to be neglected in our models.

5.2.2 Initial temperature, high effective ion charge

Next we consider the case with a high effective ion charge $Z_{\text{eff}} = 20$ in Figure 5.3. The final temperature T_{final} was again 100 eV and T_{initial} was varied between 2 and 17.5 keV. The density $n_0 = 10^{21}$ m^{-3}, higher than in the previous section, was chosen to find cases with both high and low runaway generation to include in the study. Through the whole T_{initial} span shown, the numerical model now gives the final runaway population which is the closest to the CODE result. At $T_{\text{initial}} = 5$ keV, it overestimates n_{RE} by a factor of 4. At $T_{\text{initial}} = 2$ keV the relative error is around 34, but the final runaway population is very low. The first analytic model, which in the $Z_{\text{eff}} = 1$ case was very accurate, is here the worst of the three models, with an overestimation of more than an order of magnitude.

Figures 5.3(b)-(d) show the time evolution of the runaway fraction, electric field and fast current density, for the case with T_{initial} of 10 keV. Again we see that the analytic approximations initially capture the shape of the n_{RE} curve, but stay at their maximum value while the CODE result decreases by more than an order of magnitude. Recall that the assumption in the p_c definition (equation (4.35)) in the model "analytic, p_c" was that the runaway dynamics are mainly determined by the friction and isotropic acceleration by the electric field, which becomes increasingly valid when Z_{eff} is high. As we see in the pink curve in Figure 5.3(b), this alternative p_c definition improves the analytic estimation by almost an order of magnitude. The best estimate is however the numerical model, which reaches a final value very close to CODE with a relative error of 1.3. In Figure 5.3(c), we see that our analytic and numerical models reproduce the electric field given by CODE. This can be explained

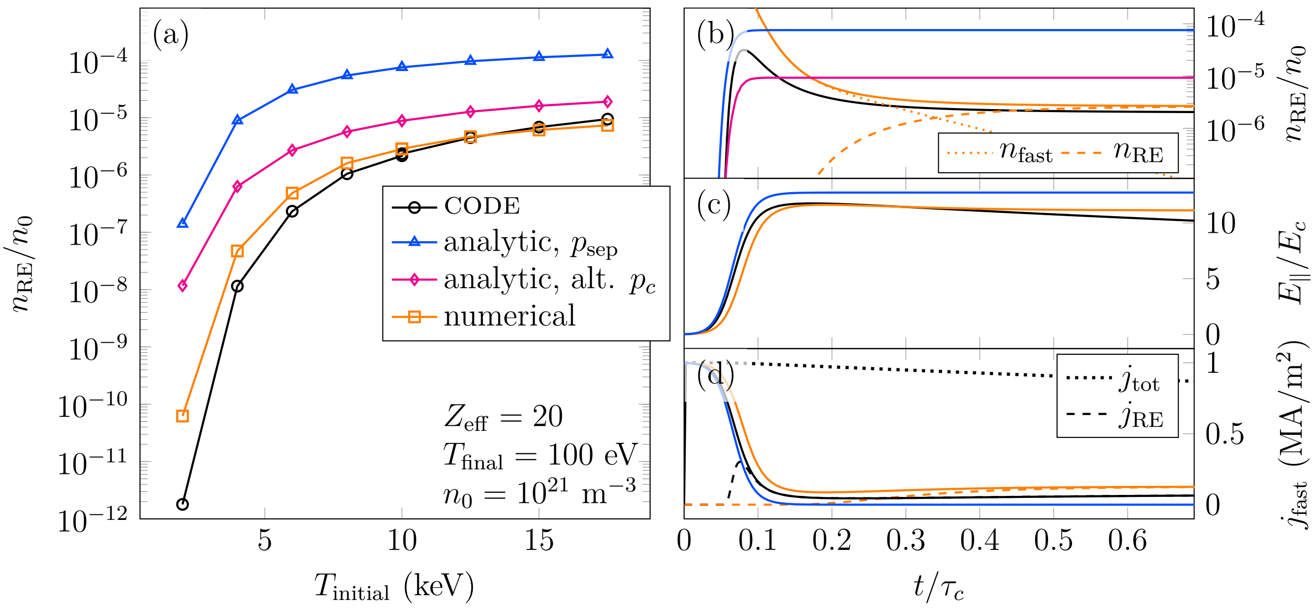

Figure 5.3: Figure (a) shows the runaway fraction obtained by CODE (black), our analytic models (blue, pink) and numerical model (orange), as a function of the pre-cooling temperature, T_{initial}. The parameters used were $Z_{\text{eff}} = 20$, $T_{\text{final}} = 100$ eV and $n_0 = 10^{21}$ m^{-3}. Figure (a) shows the final values when the pre-cooling temperature was varied. Figure (b)-(d) show the time evolution of the runaway fraction, electric field and fast current when $T_{\text{initial}} = 10$ keV.

by the low fast current in 5.3(d), which forgives the neglect of the runaway current in the analytic model. Finally, we note that the decrease in total current during the first $0.2\tau_c$ is 3 %, which we can again consider negligible.

5.2.3 Electron density

In Figure 5.4, the runaway fraction predicted by our models was compared to CODE simulations for different electron densities n_0. The temperatures used were $T_{\text{initial}} = 6$ keV and $T_{\text{final}} = 5$ eV, and were chosen to approximately resemble the ones used in previous work which used CODE to model runaway generation in argon-induced disruptions in the ASDEX Upgrade tokamak [30]. For low effective ion charge, $Z_{\text{eff}} = 1$ (solid), the runaway generation is suppressed at a density of around $6 \cdot 10^{22}$ m^{-3}. The first analytic model with a pitch-angle dependent separatrix (analytic, p_{sep}, blue) is the model which best reproduces the CODE result, with an error of less than a factor 10 when the runaway fraction is above 10^{-13}. In the lowest part of the n_0 range, $10^{21} - 10^{22}$ m^{-3}, all our models come close to the CODE result.

When a high effective ion charge was assumed, $Z_{\text{eff}} = 20$ (dashed), the density needed to suppress the runaway generation was almost an order of magnitude higher than in the $Z_{\text{eff}} = 1$ case. Here the first analytic model overestimates the runaway fraction by more than a factor of 10, even in the high conversion region around

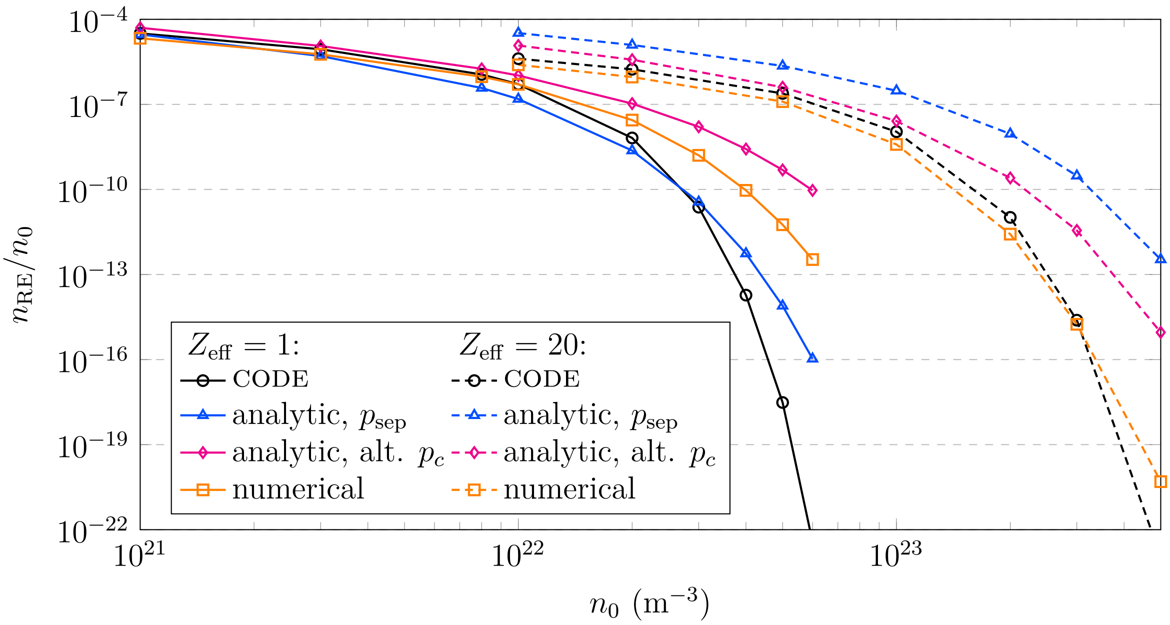

Figure 5.4: Calculated runaway fractions as a function of electron density, when the temperature was dropped from $T_{\mathrm{initial}} = 6$ keV to $T_{\mathrm{final}} = 5$ eV. The density n_0 was increased until the runaway fraction reached a very low value for $Z_{\mathrm{eff}} = 1$ (solid) and $Z_{\mathrm{eff}} = 20$ (dashed). The CODE results (black) are best approximated by the analytic solution from Section 4.1 (blue; alternative analytic model from Section 4.2 pink) when $Z = 1$, while the numerical model from Section 4.3 (orange) works better for $Z_{\mathrm{eff}} = 20$.

$n_0 = 10^{22} - 10^{23}$ m^{-3}. There, the second analytic model (analytic, alt. p_c, pink) is close to the CODE result but deviates at increased density. The numerical model works well in the whole span shown and matches the CODE values within a factor of 2 for $n_0 < 5 \cdot 10^{22}$ m^{-3} and $n_{\mathrm{RE}}/n_0 > 2 \cdot 10^{-7}$ and within a factor of 5 for $n_0 < 4 \cdot 10^{23}$ m^{-3} and $n_{\mathrm{RE}}/n_0 > 10^{-19}$.

5.2.4 Summary of parameter study

From the results presented in Sections 5.2.1-5.2.3, we see that we can capture the parameter dependence of the fraction of runaways generated with our simplified models. However, which model is the most accurate depends strongly on the choice of Z_{eff}.

For low Z_{eff}, we can conclude that our analytical model from Section 4.1, which uses a pitch-angle dependent runaway region (p_{sep}), best describes the runaway generation. The analytic approximation for the distribution function works well at early times, which we saw in Figures 5.1(b)-(c). The use of the separatrix in equation (4.19) is motivated here, since the low ion charge allows us to neglect the effect of pitch-angle scattering on the runaway dynamics. At late times the effect of the electric field can no longer be neglected, but since the analytic distribution function only contributes to the runaway generation at early times, this does not affect the final value.

For high Z_{eff}, the numerical solution well describes the final runaway fraction. As we saw in Figure 5.1(d), it correctly reproduces the distribution function at late times. The details of the runaway region are excluded from the numerical model, but as we discussed in the end of the previous chapter this becomes less important when the tail has been formed and most of the runaways are much faster than the true critical momentum.

5.3 Cooling time dependence

We recall that the models introduced in Chapter 4 all focused on a very fast thermal quench with the temperature dropping instantly from T_{initial} to T_{final}. To model a slower cooling, the model by [21], described in Section 3.3.1, uses an exponential temperature evolution. As mentioned in Section 3.3.1, this exponential temperature model has been compared to CODE simulations on a proof of concept level in [35]. Here, we extend that study to cover the sensitivity of the hot-tail generation modelling to cooling time. We investigate the impact of the two definitions of runaway region: isotropic $v > v_c = c\sqrt{E_c/E_\parallel}$ (3.21), and pitch-angle dependent $v > v_{\text{sep}}(\xi) = v_c\sqrt{2/(1+\xi)}$ (3.20).

Figure 5.5 shows the variation of the runaway fraction with cooling time, assuming the temperature has an exponential decay evolution according to equation (3.14) [21]. The CODE results (black), obtained with a self-consistent electric field evolution, are compared to the results assuming an isotropic (solid green) and pitch-angle dependent (dashed green) runaway region. For the point $t_{\text{TQ}} = 0$ we used a step function from T_{initial} to T_{final} as in Sections 5.1 and 5.2. The corresponding final runaway fractions from the analytic and numerical models there are indicated for comparison.

The cooling time t_{TQ} is normalized to the initial thermal electron collision time for the plasma τ_{ee0}, defined by equation (2.39). We note that the runaway fraction depends strongly on the choice of t_{TQ}, and in general follows our analytic or numerical model for thermal quench times below a few τ_{ee0}. For slower cooling, the runaway is in most cases well described by the exponential temperature model. We define the cutoff t_{CO} as the thermal quench time t_{TQ} for which our theoretical model equals the exponential temperature model.

The subfigures of Figure 5.5 correspond to different sets of parameters chosen to show four distinct scenarios: high (a) and low (b) conversion in the $t_{\text{TQ}} = 0$ limit when $Z_{\text{eff}} = 1$, a high-Z_{eff} case (c) and finally a case with a high final temperature (d). Figure 5.5(a) shows the runaway fraction dependence on t_{TQ}, for a parameter set where the $t_{\text{TQ}} = 0$ limit gave high conversion of the original current into runaway current. The pre-disruption plasma temperature T_{intial} was 15 keV, final temperature $T_{\text{final}} = 5$ eV and density $n_0 = 10^{22}$ m^{-3}. We find that $t_{\text{CO}} = 2.6\tau_{ee0}$,

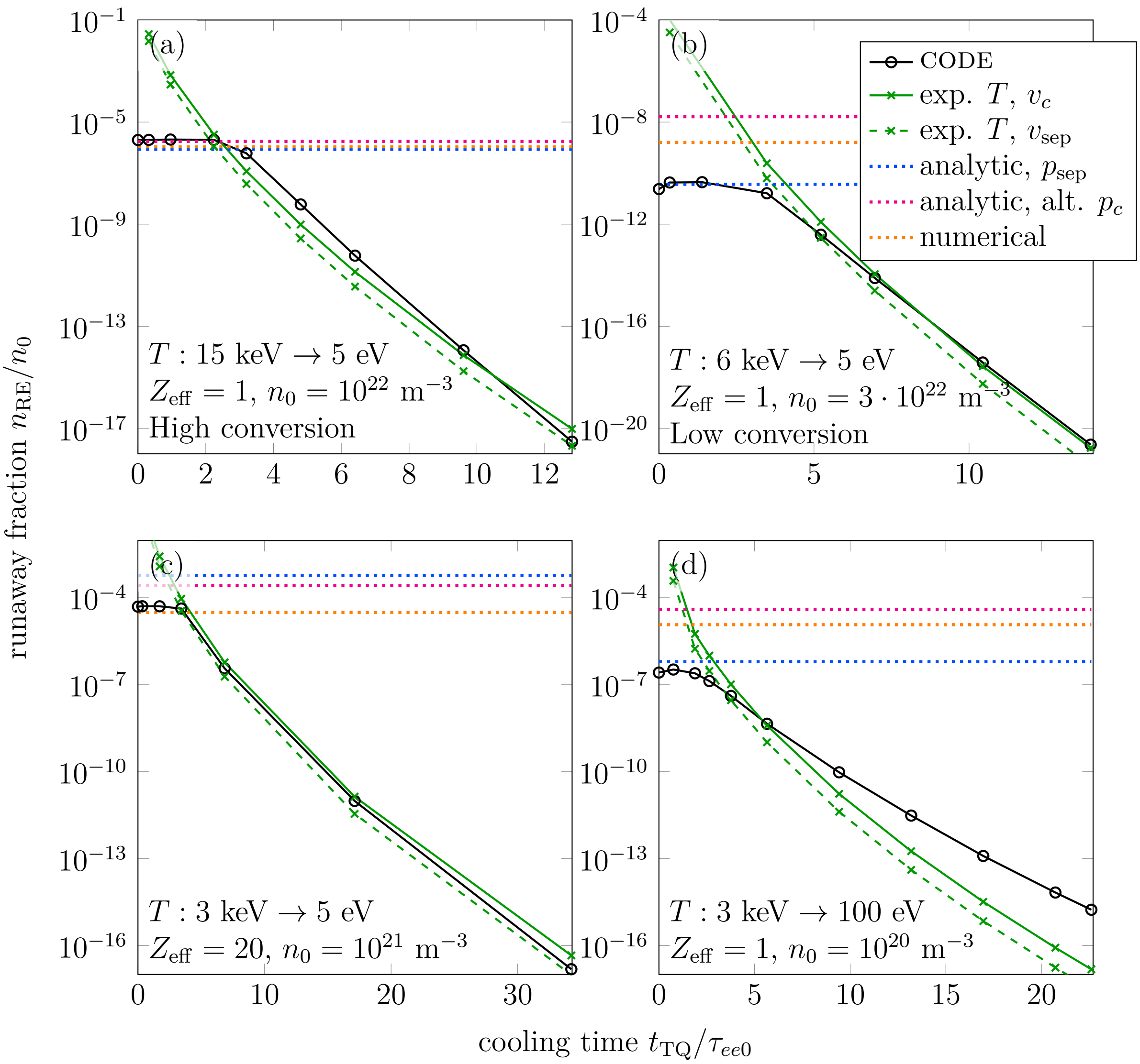

Figure 5.5: Runaway fractions for varying thermal quench times. The CODE results are shown in black, whilst the exponential temperature model is plotted in green for the ξ-dependent runaway region v_{sep} (equation (3.20), dashed) and isotropic v_c (equation (3.21), solid). The values corresponding to the $t_{TQ} = 0$ values given by the analytic and numerical models of Chapter 4 (dotted) are also indicated.

or 7 μs, below which our analytic and numerical models accurately determine the runaway fraction. This agreement was shown in Section 5.2 in the limit of $t_{\mathrm{TQ}} = 0$, but we now see that our models can be used for cooling times up to a few τ_{ee0}. For $t_{\mathrm{TQ}} > t_{\mathrm{CO}}$ the runaway fraction given by CODE decreases and follows a curve close to the exponential temperature model, which thus is a good approximation for the runaway fraction at longer cooling times. The two exponential decay solutions follow very similar paths, the only difference being that the isotropic expression (solid) always predicts 2-5 times more runaways than the ξ-dependent (dashed). This is consistent with what has been observed for an isolated case in previous work [35].

In Figure 5.5(b) we show a case with $Z_{\mathrm{eff}} = 1$, $n_0 = 3 \cdot 10^{22}$ m^{-3}, while T_{initial} and T_{final} were 6 keV and 5 eV, respectively. Note that in the $t_{\mathrm{TQ}} = 0$ limit, this corresponds to the $n_0 = 3 \cdot 10^{22}$ m^{-3} point in Figure 5.4, where the density was high enough to achieve low runaway conversion. We see a pattern similar to that in Figure 5.5(a), with $t_{\mathrm{CO}} = 4.1\tau_{ee0}$, or 1 μs, where the analytic model with a ξ-dependent runaway region (analytic, p_{sep}, dotted blue) comes closest to the CODE result at short t_{TQ}. Since $Z_{\mathrm{eff}} = 1$, this is consistent with the observations in Section 5.2. When $t_{\mathrm{TQ}} > t_{\mathrm{CO}}$, the runaway fraction decreases and approximately follows the curve calculated by the exponential decay model, and fits especially well when $t_{\mathrm{TQ}} > 7\tau_{ee0}$ where the isotropic solution (v_c) differs from CODE only by a factor of 1.5.

In Figure 5.5(c), we show a high effective ion charge case, $Z_{\mathrm{eff}} = 20$. As noted in Section 5.2, the numerical model (dotted orange) is very close to the CODE result for fast cooling at high Z_{eff}. The cutoff $t_{\mathrm{CO}} = 4.2\tau_{ee0}$ is taken as the point where the numerical model equals the exponential decay model. For $t_{\mathrm{TQ}} > t_{\mathrm{CO}}$, the runaway fraction is very well approximated by the exponential temperature decay model.

Finally, a case with a relatively high final temperature, $T_{\mathrm{final}} = 100$ eV, is shown in Figure 5.5(d). For t_{TQ} of the order of a few collision times, the analytic and exponential T models are able to approximate the CODE result within an order of magnitude, but as t_{TQ} increases the exponential T model deviates significantly from the CODE result. A similar effect was observed when T_{initial} was very low, 100 eV, see line 5 in Table 5.1. This differs from what has been observed in Figures 5.5(a)-(c), where $T_{\mathrm{final}} = 5$ eV, and verifies what was predicted in [21] and mentioned in Section 3.3.1: the assumption that diffusion can be neglected at late times only holds for sufficiently low T_{final}, so that $v \gg v_T$ is true for most of the electrons in the distribution.

A summary of the thermal quench time dependence is shown in Table 5.1. Note that the cutoff happens between 2.5 and $5\tau_{ee0}$ in all cases studied. This suggests that the runaway generation is essentially independent of the thermal quench time when t_{TQ} is below a few τ_{ee0}. When the cooling time is less than the time between two collisions, the electrons can not be slowed down during the cooling and consequently experience an instantaneous temperature drop. The electrons only start seeing the time dependent cooling when their collision time is around t_{TQ}. The cutoff happens a little above τ_{ee0} as runaway electrons on average have a higher speed than thermal electrons. Slightly higher $t_{\mathrm{CO}}/\tau_{ee0}$ above 4 are observed when $Z_{\mathrm{eff}} = 20$ and in

Table 5.1: Summary of parameters used and results from the t_{TQ} scans. The cutoff, t_{CO}, defined as the t_{TQ} for which the exponential temperature model gives the same runaway fraction as our model, are shown relative to the initial thermal collision time τ_{ee0}. If a plot of the scan is included in the thesis, the figure number is given in the final column.

Z_{eff}	T_{initial} (keV)	T_{final} (eV)	n_0 (m^{-3})	τ_{ee0} (µs)	t_{CO}/τ_{ee0}	$t_{TQ} = 0$ model	plot
1	15	5	10^{22}	3.1	2.62	analytic, p_{sep}	5.5(a)
1	6	5	$3 \cdot 10^{22}$	0.29	4.10	analytic, p_{sep}	5.5(b)
1	15	5	$2 \cdot 10^{22}$	1.8	2.49	analytic, p_{sep}	–
1	3	100	10^{20}	26	2.87	analytic, p_{sep}	5.5(d)
1	0.1	10	10^{20}	0.25	2.53	analytic, p_{sep}	–
20	3	5	10^{21}	2.9	4.15	numerical	5.5(c)
20	6	5	10^{23}	0.083	4.93	numerical	–

a $Z_{\text{eff}} = 1$ case with a lower initial temperature compared to otherwise similar scenarios. The reason for this variation is not obvious. A possible explanation could be that the hot-tail electrons in these cases are further above the thermal speed. However, a further analysis of the dependence on the different parameters is needed to draw further conclusions about this.

6
Conclusions

Electron runaway in plasmas is an interesting and important phenomenon. Runaways pose a particular problem in commercialization of fusion due to the severe damage they can cause to the inner wall of a tokamak. For runaway mitigation to be possible, we need efficient models to describe the generation of runaway electrons.

During a tokamak disruption, the temperature drops rapidly and so does the plasma conductivity. This causes the electric field to increase, which accelerates the fast electrons in the distribution. Due to the low collision frequency for fast electrons, a hot tail remains in the distribution and contributes to an increased number of electrons being accelerated. This process is called hot-tail generation, and is the dominant source of primary runaway electrons in rapidly cooling fusion plasmas.

In this thesis we derived different mathematical models to describe hot-tail runaway generation, with the purpose to develop computationally cheap calculations that can be used in combination with more extensive frameworks. The runaway fractions calculated by these models have been benchmarked against the numerical simulation tool CODE, testing sensitivity to effective ion charge, initial plasma temperature and density.

In low effective charge cases, which would correspond to an unmitigated disruption or mitigation by deuterium injection, the model that provided the best estimate was the analytic model from Section 4.1. The assumption that the electric field acceleration only has a small effect on the electron distribution during the time relevant for runaway generation was in this case valid. We were therefore able to use a simple, analytic expression for the distribution function to progress the analysis. However, when a higher effective ion charge is used, this analytical model overestimates the runaway generation by orders of magnitude. We extended the analytical model by introducing an alternative runaway region more relevant for strong pitch-angle scattering, which partly improved the runaway prediction in high effective charge cases.

The treatment was then generalized in Section 4.3 to better incorporate the effect of the increased electric field on the electron distribution. This required a numerical calculation of the distribution function, and allowed for a better treatment of the current carried by the fast electron population. In cases with a high effective charge, corresponding to a high density of injected impurities with high nuclear charge, this numerical model well captures the hot-tail generation.

We have also verified that the hot-tail generation from slow cooling is well described by previous models from the literature. When the cooling time is below a few thermal collision times of the initial plasma, however, the fast electrons do not notice a gradual decrease of the temperature but experience the cooling as instantaneous.

In CODE, the collision operator is linearized by assuming the electron distribution function to be close to a Maxwellian. In the situations of rapid cooling that we have considered in this thesis, the distribution function deviates significantly from a Maxwellian. A possible inaccuracy in the CODE results due to this has not been considered.

All the models we have implemented in this thesis require a pre-assumed temperature evolution for the cooling. As we know from the literature, the thermal quench time varies between experiments and depends on the cooling mechanism and the initial plasma parameters. For example, if the cooling is caused mainly by radiation from ionized impurities, a high initial temperature will cause a short thermal quench since the impurities are deposited more quickly into the plasma. As we saw in Chapter 5, the thermal quench time significantly affects the runaway fraction that is generated in a disruption. A proper description of the cooling is therefore needed to determine the runaway generation.

We have examined the two limits of very low and very high effective ion charge. Since real cases are somewhere between these limits, it would be desirable to find a model which works for arbitrary ion charges. This is most likely to be achieved by improving the numerical model to work for lower effective ion charges. We have seen that the anisotropy caused by the electric field cannot generally be treated as a small correction to the distribution function. Since the current theory only allows for an analytic solution in cases with small anisotropies, the kinetic equation must be solved numerically to properly include the electric field. We saw that our numerical model worked well for high effective charges, and see the potential to improve it for low-Z_{eff} scenarios. Solving the problem numerically would also allow for more generalized cases such as a varying electron density and the more accurate treatment of partial screening of ionized impurities. Improvements of our numerical model could include using the generalized collision frequencies to incorporate screening effects.

Bibliography

[1] W. Moomaw, F. Yamba, M. Kamimoto, L. Maurice, J. Nyboer, K. Urama, T. Weir, T. Bruckner, A. Jäger-Waldau, V. Krey, and et al., *Renewable Energy Sources and Climate Change Mitigation: Special Report of the Intergovernmental Panel on Climate Change*, p. 161–208. Cambridge University Press, 2011.

[2] ITER organization, 2020 (accessed May 26, 2020). `www.iter.org`.

[3] E. M. Hollmann, P. B. Aleynikov, T. Fülöp, D. A. Humphreys, V. A. Izzo, M. Lehnen, V. E. Lukash, G. Papp, G. Pautasso, F. Saint-Laurent, and J. A. Snipes, "Status of research toward the ITER disruption mitigation system," *Physics of Plasmas*, vol. 22, no. 2, p. 021802, 2015.

[4] J. P. Freidberg, *Plasma Physics and Fusion Energy.* Cambridge University Press, 2007.

[5] F. Chen, *Introduction to Plasma Physics and Controlled Fusion.* Plenum Press, 1974.

[6] J. Wesson, *Tokamaks.* Oxford University Press, 4 ed., 2011.

[7] EUROfusion, 2020 (accessed June 6, 2020). `www.euro-fusion.org`.

[8] T. Hender, J. Wesley, J. Bialek, A. Bondeson, A. Boozer, R. Buttery, A. Garofalo, T. Goodman, R. Granetz, Y. Gribov, O. Gruber, M. Gryaznevich, G. Giruzzi, S. Günter, N. Hayashi, P. Helander, C. Hegna, D. Howell, D. Humphreys, and M. Group, "Chapter 3: MHD stability, operational limits and disruptions," *Nuclear Fusion*, vol. 47, p. S128, 2007.

[9] A. Gurevich, G. Milikh, and R. Roussel-Dupre, "Runaway electron mechanism of air breakdown and preconditioning during a thunderstorm," *Physics Letters A*, vol. 165, no. 5, pp. 463 – 468, 1992.

[10] P. Helander, L.-G. Eriksson, and F. Andersson, "Runaway acceleration during magnetic reconnection in tokamaks," *Plasma Physics and Controlled Fusion*, vol. 44, no. 12B, pp. B247–B262, 2002.

[11] J. R. Dwyer, L. M. Coleman, R. Lopez, Z. Saleh, D. Concha, M. Brown, and H. K. Rassoul, "Runaway breakdown in the jovian atmospheres," *Geophysical Research Letters*, vol. 33, no. 22, 2006.

[12] C. Reux, V. Plyusnin, B. Alper, D. Alves, B. Bazylev, E. Belonohy, A. Boboc, S. Brezinsek, I. Coffey, J. Decker, P. Drewelow, S. Devaux, P. de Vries, A. Fil, S. Gerasimov, L. Giacomelli, S. Jachmich, E. Khilkevitch, V. Kiptily, R. Koslowski, U. Kruezi, M. Lehnen, I. Lupelli, P. Lomas, A. Manzanares, A. M. D. Aguilera, G. Matthews, J. Mlynář, E. Nardon, E. Nilsson, C. P. von Thun, V. Riccardo, F. Saint-Laurent, A. Shevelev, G. Sips, and C. S. and, "Runaway electron beam generation and mitigation during disruptions at JET-ILW," *Nuclear Fusion*, vol. 55, no. 9, p. 093013, 2015.

[13] B. Esposito, L. Boncagni, P. Buratti, D. Carnevale, F. Causa, M. Gospodarczyk, J. Martin-Solis, Z. Popovic, M. Agostini, G. Apruzzese, W. Bin, C. Cianfarani, R. D. Angelis, G. Granucci, A. Grosso, G. Maddaluno, D. Marocco, V. Piergotti, A. Pensa, S. Podda, G. Pucella, G. Ramogida, G. Rocchi, M. Riva, A. Sibio, C. Sozzi, B. Tilia, O. Tudisco, and M. V. and, "Runaway electron generation and control," *Plasma Physics and Controlled Fusion*, vol. 59, p. 014044, nov 2016.

[14] J. Mlynar, O. Ficker, E. Macusova, T. Markovic, D. Naydenkova, G. Papp, J. Urban, M. Vlainic, P. Vondracek, V. Weinzettl, O. Bogar, D. Bren, D. Carnevale, A. Casolari, J. Cerovsky, M. Farnik, M. Gobbin, M. Gospodarczyk, M. Hron, P. Kulhanek, J. Havlicek, A. Havranek, M. Imrisek, M. Jakubowski, N. Lamas, V. Linhart, K. Malinowski, M. Marcisovsky, E. Matveeva, R. Panek, V. V. Plyusnin, M. Rabinski, V. Svoboda, P. Svihra, J. Varju, and J. Z. and, "Runaway electron experiments at COMPASS in support of the EUROfusion ITER physics research," *Plasma Physics and Controlled Fusion*, vol. 61, no. 1, p. 014010, 2018.

[15] C. Paz-Soldan, N. Eidietis, E. Hollmann, P. Aleynikov, L. Carbajal, W. Heidbrink, M. Hoppe, C. Liu, A. Lvovskiy, D. Shiraki, D. Spong, D. Brennan, C. Cooper, D. del Castillo-Negrete, X. Du, O. Embréus, T. Fülöp, J. Herfindal, R. Moyer, P. Parks, and K. Thome, "Recent DIII-D advances in runaway electron measurement and model validation," *Nuclear Fusion*, vol. 59, no. 6, p. 066025, 2019.

[16] G. Pautasso, M. Dibon, M. G. Dunne, R. Dux, E. Fable, P. Lang, O. Linder, A. Mlynek, G. Papp, M. Bernert, A. Gude, M. Lehnen, P. J. McCarthy, and J. Stober, "Generation and dissipation of runaway electrons in ASDEX Upgrade experiments," *Nuclear Fusion*, 2020.

[17] H. Dreicer, "Electron and ion runaway in a fully ionized gas. i," *Phys. Rev.*, vol. 115, pp. 238–249, 1959.

[18] H. Dreicer, "Electron and ion runaway in a fully ionized gas. ii," *Phys. Rev.*, vol. 117, pp. 329–342, 1960.

[19] Y. Sokolov, "Multiplication of accelerated electrons in a tokamak," *JETP Letters*, vol. 29, no. 4, p. 218, 1979.

[20] M. Rosenbluth and S. Putvinski, "Theory for avalanche of runaway electrons in tokamaks," *Nuclear Fusion*, vol. 37, no. 10, pp. 1355–1362, 1997.

[21] H. M. Smith and E. Verwichte, "Hot tail runaway electron generation in tokamak disruptions," *Physics of Plasmas*, vol. 15, no. 7, p. 072502, 2008.

[22] R. W. Harvey, V. S. Chan, S. C. Chiu, T. E. Evans, M. N. Rosenbluth, and D. G. Whyte, "Runaway electron production in DIII-D killer pellet experiments, calculated with the CQL3D/KPRAD model," *Physics of Plasmas*, vol. 7, no. 11, pp. 4590–4599, 2000.

[23] P. Helander, H. Smith, T. Fülöp, and L.-G. Eriksson, "Electron kinetics in a cooling plasma," *Physics of Plasmas*, vol. 11, no. 12, pp. 5704–5709, 2004.

[24] H. Smith, P. Helander, L.-G. Eriksson, and T. Fülöp, "Runaway electron generation in a cooling plasma," *Physics of Plasmas*, vol. 12, no. 12, p. 122505, 2005.

[25] H. Nuga, M. Yagi, and A. Fukuyama, "Fokker-Planck simulation of runaway electron generation in disruptions with the hot-tail effect," *Physics of Plasmas*, vol. 23, no. 6, p. 062506, 2016.

[26] H. Nuga, A. Matsuyama, M. Yagi, and A. Fukuyama, "Fokker-Planck simulation study of hot-tail effect on runaway electron generation in ITER disruptions," *Plasma and Fusion Research*, vol. 11, 2016.

[27] L. Zeng, H. R. Koslowski, Y. Liang, A. Lvovskiy, M. Lehnen, D. Nicolai, J. Pearson, M. Rack, P. Denner, K. Finken, and K. Wongrach, "Experimental observation of hot tail runaway electron generation in TEXTOR disruptions," *Journal of Plasma Physics*, vol. 81, pp. 1–10, 2015.

[28] C. Paz-Soldan, P. Aleynikov, E. Hollmann, A. Lvovskiy, I. Bykov, X. Du, N. Eidietis, and D. Shiraki, "Runaway electron seed formation at reactor-relevant temperature," *Nuclear Fusion*, vol. 60, no. 5, p. 056020, 2020.

[29] A. Stahl, *Momemtum-space dynamics of runaway electrons in plasmas.* PhD thesis, Chalmers University of Technology, 2017.

[30] K. Insulander Björk, G. Papp, O. Embréus, L. Hesslow, T. Fülöp, O. Vallhagen, A. Lier, G. Pautasso, and A. Bock, "Kinetic modelling of runaway electron generation in argon-induced disruptions in ASDEX Upgrade," 2020.

[31] B. Breizman, P. Aleynikov, E. Hollmann, and M. Lehnen, "Physics of runaway electrons in tokamaks," *Nuclear Fusion*, vol. 59, 2019.

[32] ITER Physics Basis Editors and ITER Physics Expert Group Chairs an Co-Chairs and ITER Joint Central Team and Physics Unit, "Chapter 1: Overview and summary," *Nuclear Fusion*, vol. 39, no. 12, pp. 2137–2174, 1999.

[33] L. Hesslow, O. Embréus, O. Vallhagen, and T. Fülöp, "Influence of massive material injection on avalanche runaway generation during tokamak disruptions," *Nuclear Fusion*, vol. 59, no. 8, p. 084004, 2019.

[34] M. Landreman, A. Stahl, and T. Fülöp, "Numerical calculation of the runaway electron distribution function and associated synchrotron emission," *Computer Physics Communications*, vol. 185, p. 847–855, 2014.

[35] A. Stahl, O. Embréus, G. Papp, M. Landreman, and T. Fülöp, "Kinetic modelling of runaway electrons in dynamic scenarios," *Nuclear Fusion*, vol. 56, no. 11, p. 112009, 2016.

[36] T. Fehér, H. M. Smith, T. Fülöp, and K. Gál, "Simulation of runaway electron generation during plasma shutdown by impurity injection in ITER," *Plasma Physics and Controlled Fusion*, vol. 53, no. 3, p. 035014, 2011.

[37] H. M. Smith, T. Fehér, T. Fülöp, K. Gál, and E. Verwichte, "Runaway electron generation in tokamak disruptions," *Plasma Physics and Controlled Fusion*, vol. 51, no. 12, p. 124008, 2009.

[38] T. Fülöp, H. M. Smith, and G. Pokol, "Magnetic field threshold for runaway generation in tokamak disruptions," *Physics of Plasmas*, vol. 16, no. 2, p. 022502, 2009.

[39] J. R. Martín-Solís, A. Loarte, and M. Lehnen, "Formation and termination of runaway beams in ITER disruptions," *Nuclear Fusion*, vol. 57, no. 6, p. 066025, 2017.

[40] P. Helander and D. Sigmar, *Collisional Transport in Magnetized Plasmas.* Cambridge Monographs on Plasma Physics, Cambridge University Press, 2005.

[41] J. D. Callen, "Coulomb collisions," in *Fundamentals of Plasma Physics*, ch. 2, 2006.

[42] L. Hesslow, O. Embréus, M. Hoppe, T. DuBois, G. Papp, M. Rahm, and T. Fülöp, "Generalized collision operator for fast electrons interacting with partially ionized impurities," *Journal of Plasma Physics*, vol. 84, no. 6, p. 905840605, 2018.

[43] R. J. Goldston and P. H. Rutherford, *Introduction to Plasma Physics.* CRC Press, 1995.

[44] A. Kuritsyn, M. Yamada, S. Gerhardt, H. Ji, R. Kulsrud, and Y. Ren, "Measurements of the parallel and transverse Spitzer resistivities during collisional magnetic reconnection," *Physics of Plasmas*, vol. 13, no. 5, p. 055703, 2006.

[45] L. Hesslow, O. Embréus, G. J. Wilkie, G. Papp, and T. Fülöp, "Effect of partially ionized impurities and radiation on the effective critical electric field for runaway generation," *Plasma Physics and Controlled Fusion*, vol. 60, no. 7, p. 074010, 2018.

[46] P. Sandquist, S. E. Sharapov, P. Helander, and M. Lisak, "Relativistic electron distribution function of a plasma in a near-critical electric field," *Physics of Plasmas*, vol. 13, no. 7, p. 072108, 2006.

[47] L. Hesslow, O. Embréus, A. Stahl, T. DuBois, G. Papp, S. Newton, and T. Fülöp, "Effect of partially screened nuclei on fast-electron dynamics," *Physical Review Letters*, vol. 118, p. 255001, 2017.

[48] J. Connor and R. Hastie, "Relativistic limitations on runaway electrons," *Nuclear Fusion*, vol. 15, no. 3, pp. 415–424, 1975.

[49] L. Hesslow, L. Unnerfelt, O. Vallhagen, O. Embréus, M. Hoppe, G. Papp, and T. Fülöp, "Evaluation of the Dreicer runaway generation rate in the presence of high-Z impurities using a neural network," *Journal of Plasma Physics*, vol. 85, p. 475850601, 2019.

[50] O. Embréus, A. Stahl, and T. Fülöp, "On the relativistic large-angle electron collision operator for runaway avalanches in plasmas," *Journal of Plasma Physics*, vol. 84, no. 1, p. 905840102, 2018.

[51] H. M. Smith, T. Fehér, T. Fülöp, K. Gál, and E. Verwichte, "Runaway electron generation in tokamak disruptions," *Plasma Physics and Controlled Fusion*, vol. 51, no. 12, p. 124008, 2009.

[52] G. Papp, M. Drevlak, T. Fülöp, and P. Helander, "Runaway electron drift orbits in magnetostatic perturbed fields," *Nuclear Fusion*, vol. 51, no. 4, p. 043004, 2011.

[53] P. Aleynikov and B. N. Breizman, "Generation of runaway electrons during the thermal quench in tokamaks," *Nuclear Fusion*, vol. 57, no. 4, p. 046009, 2017.

A

Rewriting the kinetic equation

We show here that the kinetic equation (3.24) used in Section 3.3.2 and [53] is equivalent to equation (4.1), which we solve in Chapter 4. We start with equation (3.24)

$$\frac{\partial F}{\partial s} + \frac{\partial}{\partial p}\left[E\cos\theta - 1 - \frac{1}{p^2}\right]F = \frac{1}{\sin\theta}\frac{\partial}{\partial\theta}\sin\theta\left[E\frac{\sin\theta}{p}F + \frac{(Z_{\text{eff}}+1)}{2}\frac{\sqrt{p^2+1}}{p^3}\frac{\partial F}{\partial\theta}\right]. \quad (A.1)$$

and rearrange the terms

$$\begin{aligned}\frac{\partial F}{\partial s} &+ E\left(\frac{\partial}{\partial p}\left[\cos\theta F\right] - \frac{1}{\sin\theta}\frac{\partial}{\partial\theta}\left[\frac{\sin^2\theta}{p}F\right]\right)\\ &= \frac{\partial}{\partial p}\left[\frac{(p^2+1)}{p^2}F\right] + \frac{(Z_{\text{eff}}+1)}{2}\frac{\sqrt{p^2+1}}{p^3}\frac{1}{\sin\theta}\frac{\partial}{\partial\theta}\left[\sin\theta\frac{\partial F}{\partial\theta}\right],\end{aligned} \quad (A.2)$$

where $F = 2p^2 f$, $\cos\theta = \xi$ and $\frac{\partial s}{\partial t} = \frac{1}{\tau_c}$. With $\frac{1}{\sin\theta}\frac{\partial}{\partial\theta} = -\frac{\partial}{\partial\xi}$ and $\sin^2\theta = 1-\xi^2$, the expression inside the first parenthesis is rewritten to

$$\begin{aligned}2\xi\frac{\partial(p^2 f)}{\partial p} + 2p\frac{\partial}{\partial\xi}\left[(1-\xi^2)f\right] &=\\ 2\xi\left(2pf + p^2\frac{\partial f}{\partial p}\right) + 2p\left((-2\xi)f + (1-\xi^2)\frac{\partial f}{\partial\xi}\right) &= 2p^2\left(\xi\frac{\partial f}{\partial p} + \frac{1-\xi^2}{p}\frac{\partial f}{\partial\xi}\right).\end{aligned} \quad (A.3)$$

The θ part in the last term of equation (A.2) becomes

$$-\frac{\partial}{\partial\xi}\left[-(1-\xi^2)\frac{\partial(2p^2 f)}{\partial\xi}\right] = 2p^2\frac{\partial}{\partial\xi}\left[(1-\xi^2)\frac{\partial f}{\partial\xi}\right]. \quad (A.4)$$

Inserting $\frac{\partial}{\partial s} = \tau_c\frac{\partial}{\partial t}$, (A.3) and (A.4) in (A.2) yields

$$\begin{aligned}2p^2\tau_c\frac{\partial f}{\partial t} &+ 2p^2 E\left(\xi\frac{\partial f}{\partial p} + \frac{1-\xi^2}{p}\frac{\partial f}{\partial\xi}\right)\\ &= 2\frac{\partial}{\partial p}\left[(p^2+1)f\right] + 2p^2\frac{(Z_{\text{eff}}+1)}{2}\frac{\sqrt{p^2+1}}{p^3}\frac{\partial}{\partial\xi}\left[(1-\xi^2)\frac{\partial f}{\partial\xi}\right].\end{aligned} \quad (A.5)$$

Now, dividing by $2p^2$ and inserting $\gamma = \sqrt{1+p^2}$, we get

$$\tau_c\frac{\partial f}{\partial t} + E\left(\xi\frac{\partial f}{\partial p} + \frac{1-\xi^2}{p}\frac{\partial f}{\partial\xi}\right) = \frac{1}{p^2}\frac{\partial}{\partial p}\left[\gamma^2 f\right] + \frac{(Z_{\text{eff}}+1)}{2}\frac{\gamma}{p^3}\frac{\partial}{\partial\xi}\left[(1-\xi^2)\frac{\partial f}{\partial\xi}\right], \quad (A.6)$$

which is the same as equation (4.1) when $\bar{\nu}_S = 1$ and $\bar{\nu}_D = 1 + Z_{\text{eff}}$.

B

Lower boundary of the runaway region

As we mention in the end of Chapter 4, the final value of the runaway fraction is insensitive to the details of the lower boundary of the runaway region when the tail of hot electrons in the distribution is modelled correctly. Here we show an example where this is the case. Figure B.1 shows the result of a CODE simulation where the runaway fraction was calculated using different definitions for the runaway region. The separatrix, p_{sep}, and the isotropic boundary, p_c, depend on the electric field and are defined by equations (3.6) and (3.5) respectively. We also show three curves with constant critical momenta. As the figure shows, the different runaway regions give very different runaway fractions initially, but eventually stabilize around the same value.

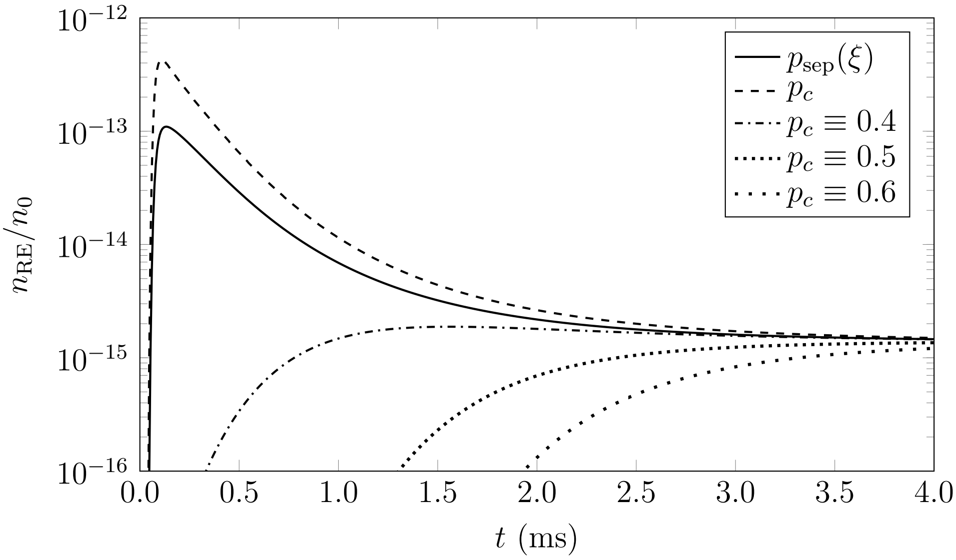

Figure B.1: Runaway fractions calculated using different definitions for the runaway region. In this example we used the parameters $T_{\mathrm{initial}} = 10$ keV, $T_{\mathrm{final}} = 100$ eV, $Z_{\mathrm{eff}} = 1$, and $n_0 = 10^{20}$ m^{-3}.